Quantum state tomography of large nuclear spins in a semiconductor quantum well: Optimal robustness against errors as quantified by condition numbers

Adam Miranowicz,[1,2] Şahin K. Özdemir,[1,3,7] Jiří Bajer,[4] Go Yusa,[5,6] Nobuyuki Imoto,[7]
Yoshiro Hirayama,[6,8] and Franco Nori[1,9]

[1]*CEMS, RIKEN, 351-0198 Wako-shi, Japan*
[2]*Faculty of Physics, Adam Mickiewicz University, PL-61-614 Poznań, Poland*
[3]*Department of Electrical and Systems Engineering, Washington University, St. Louis, Missouri 63130, USA*
[4]*Department of Optics, Palacký University, 772 00 Olomouc, Czech Republic*
[5]*PRESTO-JST, Honmachi, Kawaguchi, 331-0012 Saitama, Japan*
[6]*Department of Physics, Tohoku University, Sendai, 980-8578 Miyagi, Japan*
[7]*Graduate School of Engineering Science, Osaka University, Toyonaka, Osaka 560-8531, Japan*
[8]*ERATO Nuclear Spin Electronics Project, Aramaki, Aza Aoba, Sendai 980-0845, Japan*
[9]*Department of Physics, The University of Michigan, Ann Arbor, Michigan 48109-1040, USA*

We discuss methods of quantum state tomography for solid-state systems with a large nuclear spin $I = 3/2$ in nanometer-scale semiconductors devices based on a quantum well. Due to quadrupolar interactions, the Zeeman levels of these nuclear-spin devices become nonequidistant, forming a controllable four-level quantum system (known as quartit or ququart). The occupation of these levels can be selectively and coherently manipulated by multiphoton transitions using the techniques of nuclear magnetic resonance (NMR) [Yusa *et al.*, Nature (London) **434**, 1001 (2005)]. These methods are based on an unconventional approach to NMR, where the longitudinal magnetization M_z is directly measured. This is in contrast to the standard NMR experiments and tomographic methods, where the transverse magnetization M_{xy} is detected. The robustness against errors in the measured data is analyzed by using the condition number based on the spectral norm. We propose several methods with optimized sets of rotations yielding the highest robustness against errors, as described by the condition number equal to 1, assuming an ideal experimental detection. This robustness is only slightly deteriorated, as given by the condition number equal to 1.05, for a more realistic "noisy" M_z detection based on the standard cyclically ordered phase sequence (CYCLOPS) method.

I. INTRODUCTION

Quantum state engineering has been attracting increasing attention in fundamental physics research as well as in applications in quantum cryptography, quantum communication, and, potentially, quantum information processing (QIP) [1]. Quantum state engineering provides methods for synthesis of quantum states and their coherent control and characterization. The latter task can be realized by quantum state and process tomographic methods.

Quantum state tomography (QST) is a method for reconstruction of a quantum state in a series of measurements performed on an ensemble of identical quantum states. *Quantum process tomography* (QPT) is a method, closely related to QST, which enables a complete characterization of the dynamics of a quantum system. Both QST and QPT have been applied widely to QIP in finite- and infinite-dimensional optical systems (for reviews see Refs. [2,3] and references therein). In particular, much work has been on QST of polarization states of photons (see, e.g., Refs. [4–8]), homodyne QST [9], and homodyne QPT [10,11] probed with coherent states. Other examples include QST in superconducting circuits [12,13]. QST has also been applied in nuclear-spin systems using nuclear magnetic resonance (NMR) spectroscopy, which was motivated by quantum information interest [14,15]. The NMR QST and NMR QPT were first developed for liquid-state nuclear spin-1/2 systems [15] and only later applied both

to liquid- and solid-state systems of quadrupolar nuclei of spin-3/2 [16–19] and spin-7/2 [20].

The use of multilevel systems (so-called *qudits*) instead of two-level systems (qubits) is an alternative paradigm [21,22] in QIP, which has attracted attention in recent years. Standard examples of higher-order nuclear spins I include: $I = 3/2$ for the isotopes ^{69}Ga, ^{71}Ga, and ^{75}As (in, e.g., GaAs); $I = 5/2$ for ^{27}Al (in, e.g., AlN) or ^{121}Sb (in, e.g., FeSb$_2$); $I = 7/2$ for ^{123}Sb (also in FeSb$_2$); as well as $I = 9/2$ for ^{113}In and ^{115}In (in, e.g., InAs, InSb, and InP) and ^{73}Ge. Note that large nuclear spins occur also in molecular magnets, i.e., clusters of spins, which can be applied for QIP [23,24]. As another example, the superconducting circuits in Ref. [21] have up to five levels and can model rotations of spin-1 and spin-3/2. Here, we will focus solely on QIP using quadrupolar nuclei with spin-3/2, which are equivalent to a four-level system.

Another motivation for the application of qudits for QIP is related to an important question concerning the scalability of two qubits to many qubits. If one simply plans to increase the number N of qubits, then the required numbers of levels scales up exponentially. This becomes very hard to implement when N is large. However, some ordinary classical computers are not assembled with simple AND, NAND, OR, and NOT gates, but instead they are constructed using higher-level logic gates. Similarly, quantum computers might be constructed with slightly more complex logic gates, rather than, e.g.,

only single-qubit rotations and CNOT gates. In this direction, multilevel systems are helpful.

A word of caution: Replacing qubits by qudits causes a faster exponential divergence in the number of levels, and thus one loses the advantage of "using a single multi-level system" over "using many two-level systems." Thus, this approach should be applied carefully. Indeed, using qudits could reduce the complexity of quantum computers (see Ref. [21] and the justifications given there). Moreover, for qudits, there are optimal recipes for gate operations (see Sec. III) and quantum tomography methods to be discussed in the following sections.

Various two-qubit quantum state engineering methods and quantum algorithms have been realized in NMR experiments with spin-3/2 systems. Examples include: the demonstration of classical [25–27] and quantum [16,17,28,29] gates, generation of Bell states [28,29], the quantum Fourier transform [17], and implementations of simple quantum algorithms (i.e., the two-qubit Grover search algorithm [17,30] and the Deutsch-Jozsa algorithm [17,31]). The existence of quantum correlations (as revealed by quantum discord) was also experimentally demonstrated in spin-3/2 systems (see, e.g., Ref. [32]). It is worth noting that a prerequisite for the realization of all these gates and algorithms is the preparation of pseudopure states (see also Refs. [14,33,34] and references therein).

Quadrupolar nuclei with spin-7/2 have also attracted increasing interest, as it is highly desirable to scale QIP beyond two (real or virtual) qubits. A few NMR experiments were performed with spin-7/2 systems, e.g., the preparation of effective pure states [35], a quantum simulation [36], a half-adder and subtractor operations [27,37], a test of phase coherence in electromagnetically induced transparency [38], and three-qubit Deutsch-Jozsa algorithms [20,39,40]. A complete verification of the generated states and/or performed algorithms in the aforementioned experiments requires the application of QST.

In this article, we describe QST methods for an unconventional approach to NMR (sometimes referred to as "exotic NMR") in semiconductor nanostructures [33,41–44], which is based on the measurement of the longitudinal magnetization M_z.

In contrast to this approach, the vast majority of the NMR tomographic methods are based on conventional (standard) NMR experiments, where the transverse magnetization M_{xy} is detected. Indeed, a very tiny magnetic field produced by the nuclear spin rotation in the xy plane with a resonant frequency is picked up by a surrounding coil. In this method, the M_{xy} component is measured by using induction detection (M_{xy} detection). However, this widely used conventional NMR suffers from low sensitivity arising from induction detection, so one should prepare large volume samples occasionally reaching a qubic centimeter (at least a qubic millimeter). In the application to semiconductor (solid-state) systems (see Ref. [45] and references therein), multiple-layer quantum wells with 10–100 layers should be prepared to detect clear signals with a sufficient noise-to-signal ratio. A main advantage of semiconductor (solid-state) qubits is its precise controllability by using gate operations. Such gate operation is based on a single quantum well and nanostructure so conventional NMR is obviously not appropriate for these systems. Since the mid-2000s, highly sensitive NMR methods suitable for semiconductor hetero- and nanosystems have been developed by using electrical [41,42] and optical [46] means. However, they have all relied on a direct measurement of the nuclear spin magnetization, i.e., M_z detection. Therefore, it is important for semiconductor (solid-state) nuclear-spin qubits to develop QST appropriate for the direct detection of M_z.

Here we study NMR tomography of solid-state four-level quantum systems, also known as quartits or ququarts. The main result of this paper is the proposal of various QST methods based on M_z detection, which are the most robust against errors as quantified by a condition number equal (or almost equal) to 1. Note that the proposed QST methods can be applied not solely to solid-state systems but also to liquid-state quartits. Moreover, these methods can be generalized for QST of qudits. There has also been interest in the generation and state tomography of other systems, especially optical qudits, including qutrits (i.e., three-level quantum systems) (see, e.g., Ref. [47]).

The paper is organized as follows: In Sec. II, we specify the quadrupolar interaction model. In Sec. III, we describe sequences of NMR pulses for implementing qubit gates in qudits. In Sec. IV, we present the key aspects of the M_z-based QST of a spin-3/2 system. We also briefly discuss a nanometer-scale all-electrical resistively detected NMR device [41,42], where the M_z magnetization can be measured. In Sec. V, we discuss the linear reconstruction of density matrices in relation to condition numbers describing how these methods are robust against errors. In Sec. VI, we specify the M_z-detection approaches to be applied in the next sections. These include three approaches: a theoretical approach, as well as both ideal and nonideal (noisy) experimental approaches. The main results of this paper are presented in Secs. VII–IX. Specifically, we propose various sets of rotations, which enable optimal reconstructions of all the diagonal (in Sec. VII) and off-diagonal (in Sec. VIII) elements of a spin-3/2 density matrix. These two reconstructions are combined in Sec. IX. In Sec. X, we show how to construct sets of operationally optimized rotations by finding single-photon replacements for multiphoton rotations. We conclude in Sec. XI. In the Appendices, for completeness and clarity, we define selective rotations and briefly compare the M_{xy} and M_z detections.

II. INTERACTION MODEL

First, we describe a model for large nuclear spins, in a semiconductor quantum well, which are interacting with radio-frequency (RF) pulses. A general description of such an interaction can be found in standard textbooks on NMR (see, e.g., Refs. [48,49]). In particular, the model described in detail by Leuenberger *et al.* [50], which was directly applied in the experiment of Yusa *et al.* [42], can also be adapted here.

Specifically, we analyze an ensemble of quadrupolar nuclei (with spin $I = 3/2$) in a semiconductor quantum well interacting with N RF pulses of the carrier frequency $\omega_{\mathrm{RF}}^{(k)}$, phase $\phi_{\mathrm{RF}}^{(k)}$, and magnetic-field amplitude B_k ($k = 1, 2, \ldots, N$) in the presence of a strong magnetic field B_0. The effective total Hamiltonian in the laboratory frame reads [42,48–50]

$$\mathcal{H} = \mathcal{H}_0 + \mathcal{H}_{\mathrm{int}}, \tag{1}$$
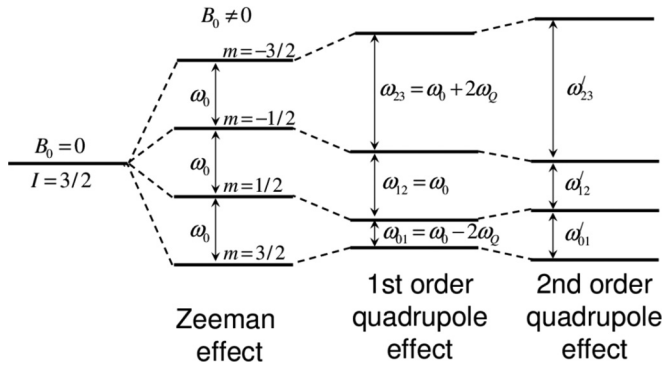
FIG. 1. Schematic diagram of the energy levels of a spin $I = 3/2$ nucleus in an external magnetic field B_0 due to Zeeman interactions with additional shifts originating from the first- and second-order quadrupole interactions. The second-order shifts completely remove the degeneracy between the levels, which is desirable for QST. Unfortunately, the second-order shifts are negligible in the nanoscale device studied here and thus will be omitted hereafter.

being a sum of the free term

$$\mathcal{H}_0 = \mathcal{H}_Z + \mathcal{H}_Q = \hbar\omega_0 I_z + \frac{\hbar\omega_Q}{3}\big[3I_z^2 - I(I+1)\big], \quad (2)$$

and the term describing the interaction of the nuclei with N pulses:

$$\mathcal{H}_{\text{int}} = \sum_{k=1}^{N} \frac{\hbar\omega_k}{2}\big[I_+ e^{-i(\omega_{\text{RF}}^{(k)}t + \phi_{\text{RF}}^{(k)})} + I_- e^{i(\omega_{\text{RF}}^{(k)}t + \phi_{\text{RF}}^{(k)})}\big]$$

$$= \sum_{k=1}^{N} \hbar\omega_k\big[I_x \cos\big(\omega_{\text{RF}}^{(k)}t + \phi_{\text{RF}}^{(k)}\big) + I_y \sin\big(\omega_{\text{RF}}^{(k)}t + \phi_{\text{RF}}^{(k)}\big)\big].$$

$$(3)$$

Here $\mathcal{H}_Z = \hbar\omega_0 I_z$ and $\mathcal{H}_Q$ describe, respectively, the Zeeman and quadrupole splittings (see Fig. 1). The operator I_α (for $\alpha = x,y,z$) is the α component of the spin angular-momentum operator, and $I_\pm = I_x \pm iI_y$. Moreover, $\omega_0 = -\gamma B_0$ is the nuclear Larmor frequency, and $\omega_k = -\gamma B_k$ is the amplitude (strength) of the kth pulse, where γ is the gyromagnetic ratio. For the example of the nuclei ^{69}Ga and ^{71}As of spin $I = 3/2$ in semiconductor GaAs, we can choose the gyromagnetic ratios to be $\gamma(^{69}\text{Ga}) = 1.17 \times 10^7\,\text{s}^{-1}\text{T}^{-1}$ and $\gamma(^{71}\text{As}) = 7.32 \times 10^6\,\text{s}^{-1}\text{T}^{-1}$, which are estimated from the spectra measured in Ref. [42]. The Hamiltonian $\mathcal{H}_Q = \mathcal{H}_Q^{(1)} + \mathcal{H}_Q^{(2)} + \cdots$ describes the quadrupolar interaction as a sum of the first- and second-order quadrupolar terms (as shown in Fig. 1) but also higher-order terms. The first-order quadrupolar splitting parameter (quadrupolar frequency) $2\omega_Q$ is given for solids by [51]:

$$\omega_Q \equiv \omega_Q^{(1)} = \frac{3\pi C_Q}{4I(2I-1)}(3\cos^2\theta_Q - 1), \quad (4)$$

where C_Q is the quadrupolar coupling constant, and θ_Q is the angle between the direction of the field B_0 and the principle axis of the electric-field gradient tensor. We assume a uniaxial electric-field gradient tensor, i.e., the biaxiality parameter is zero ($\eta_Q = 0$). Under the secular approximation, which is valid

for relatively small ω_Q, the effective interaction is described solely by the first-order quadrupolar Hamiltonian, as we have assumed in Eq. (2).

The quadrupolar frequencies are typically of the order of 10–100 kHz. For example, the values for the isotopes in semiconductor GaAs can be found in Refs. [42,50,52]. In our numerical simulations, we set the following values of the quadrupolar frequencies: $\omega_Q(^{69}\text{Ga}) = 15.2$ kHz and $\omega_Q(^{71}\text{As}) = 26.9$ kHz. These values were estimated from the experimental spectra reported in Ref. [42]. Moreover, we also choose in our simulations the same values of parameters as those measured or estimated in the experiment with nanometer-scale device in Ref. [42]. Namely $B_0 = 6.3$ T and $B_k = 0.2$–1.4 mT, and decoherence time is $T_2 \approx 1$ ms.

Let us denote the eigenvalues and eigenvectors of $\mathcal{H}_0$ by ϵ_m and $|m\rangle$, respectively, i.e., $\mathcal{H}_0|m\rangle = \epsilon_m|m\rangle$. If the condition $|\omega_k| \ll |\omega_Q| \ll |\omega_0|$ is satisfied, one can apply a selective RF pulse resonant with a transition $|m\rangle \leftrightarrow |n\rangle$, i.e., $\hbar\omega_{\text{RF}}^{(k)} = \epsilon_m - \epsilon_n$, where $m,n = 0,1,\ldots$. One can also analyze N-photon resonant transitions, which correspond to the condition $N\hbar\omega_{\text{RF}}^{(k)} = \epsilon_m - \epsilon_n$, where $k = 1,2,\ldots$ (see Fig. 2). Note that Eq. (4) can still be used, even if the $\omega_{\text{RF}}^{(k)}$ are slightly detuned from the resonant frequencies by $\delta\omega_k$.

In the more general case when N RF pulses of different frequencies $\omega_{\text{RF}}^{(k)}$ are applied simultaneously, then clearly the *standard* rotating frame is not useful to transform the time-dependent Hamiltonian, given by Eq. (4), into a time-independent form. However, if the quadrupolar splitting $2\hbar\omega_Q$ is much larger than the detuning energies $\hbar\delta\omega_k$, then one can still transform Eq. (1) into a completely time-independent Hamiltonian in a *generalized* rotating frame, as described in, e.g., Ref. [50].

The Hamiltonian $\mathcal{H}$ can be transformed to the rotating frame as follows:

$$\mathcal{H}_{\text{rot}} = U\mathcal{H}U^\dagger - i\hbar U\frac{\partial U^\dagger}{\partial t}. \quad (5)$$

Let us assume that only a single pulse ($k = 1$) is applied of strength ω_1, frequency $\omega_{\text{RF}} \equiv \omega_{\text{RF}}^{(1)}$, and phase $\phi \equiv \phi_{\text{RF}}^{(1)}$. Then
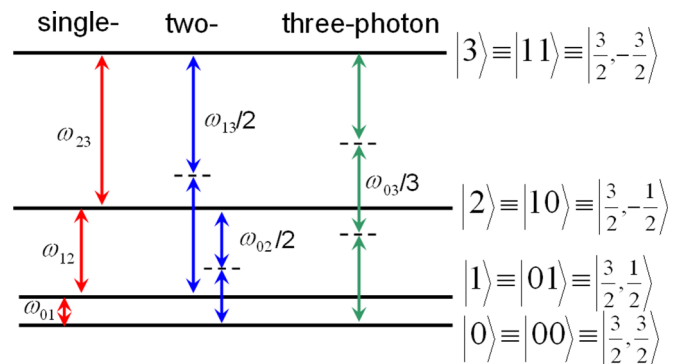

FIG. 2. (Color online) A quartit (a spin-3/2 nucleus) is formally equivalent to two qubits (two spin-1/2 nuclei), as shown here via their energy levels and their corresponding frequencies. Single-photon ($\hbar\omega_{01}, \hbar\omega_{12}, \hbar\omega_{23}$), two-photon ($\hbar\omega_{02}/2, \hbar\omega_{13}/2$), and three-photon ($\hbar\omega_{03}/3$) transitions drive single, double, and triple quantum coherent oscillations between two levels separated by one ($\Delta m = 1$), two ($\Delta m = 2$), and three ($\Delta m = 3$) quanta of angular momentum, respectively.

the time-dependent Hamiltonian, given by Eq. (1), in the frame rotating with angular frequency ω_{RF}, becomes the well-known time-independent Hamiltonian:

$$\mathcal{H}_{rot} = \hbar\Delta\omega I_z + \mathcal{H}_Q + \hbar\omega_1 I_\phi,$$
$$I_\phi = I_x \cos\phi + I_y \sin\phi = \tfrac{1}{2}(I_+ e^{-i\phi} + I_- e^{i\phi}), \quad (6)$$

where $\Delta\omega = \omega_0 - \omega_{RF}$ is the frequency offset. Equation (6) is obtained from Eqs. (1) and (5) for $U = \exp(-i\omega_{RF} I_z t)$.

The initial state (before applying pulses) of the spin system at a high temperature T can be described by

$$\rho = Z^{-1} \exp(-\beta\mathcal{H}_0) \approx Z^{-1}(1 - \beta\mathcal{H}_0), \quad (7)$$

where Z is the partition function and $\beta = 1/(k_B T)$. The term $\beta\mathcal{H}_0/Z$ corresponds to a deviation density matrix. Thus, the initial state ρ of a spin-3/2 system can be approximated by

$$\rho \approx \tfrac{1}{4}(1 - \hbar\omega_0\beta I_z), \quad (8)$$

if $|\omega_Q| \ll |\omega_0|$.

The evolution of a state, given by $\rho(t_0)$, during the application of a single pulse of strength ω_1 and duration t_p, is described in the rotating frame by:

$$\rho(t + t_p) = \mathcal{U}(\omega_1, t_p)\rho(t)\mathcal{U}^\dagger(\omega_1, t_p), \quad (9)$$

where the evolution operator is

$$\mathcal{U}(\omega_1, t) = \exp[-(i/\hbar)\mathcal{H}_{rot}t]. \quad (10)$$

The evolution of $\rho(t)$ in the absence of pulses from the time t to $t + \Delta t$ is given by:

$$\rho(t + \Delta t) = \mathcal{U}(0, \Delta t)\rho(t)\mathcal{U}^\dagger(0, \Delta t). \quad (11)$$

Analytical expressions for the evolution operator $\mathcal{U}(\omega_1, t)$ and the corresponding density matrices can be obtained by finding eigenvalues and eigenstates of $\mathcal{H}_{rot}$. For example, by assuming an RF pulse to be resonant with the central line (i.e., $\omega_{RF} = \omega_{12} = \omega_0$), and by setting $\phi = 0$, we find the following eigenvalues of $\mathcal{H}_{rot}$:

$$\text{eig}(\mathcal{H}_{rot}) = \left[\frac{\omega_1}{2} + \Omega_-, \frac{\omega_1}{2} - \Omega_-, -\frac{\omega_1}{2} - \Omega_+, -\frac{\omega_1}{2} + \Omega_+ \right], \quad (12)$$

where $\Omega_\pm = \sqrt{\omega_1^2 \pm \omega_1\omega_Q + \omega_Q^2}$. The corresponding eigenvectors of $\mathcal{H}_{rot}$ for $m = 1, 2$ and $n = 3, 4$ are equal to:

$$|V_m\rangle = \mathcal{N}_m[\sqrt{3}\omega_1(|3\rangle + |0\rangle) + y_m(|1\rangle + |2\rangle)],$$
$$|V_n\rangle = \mathcal{N}_n[\sqrt{3}\omega_1(|3\rangle - |0\rangle) + z_n(|1\rangle - |2\rangle)], \quad (13)$$

where $\mathcal{N}_m$ and $\mathcal{N}_n$ are normalization constants, and

$$y_m = \omega_1 + 2(-1)^m\Omega_- - 2\omega_Q,$$
$$z_n = \omega_1 - 2(-1)^n\Omega_+ + 2\omega_Q. \quad (14)$$

The general solution for $\mathcal{U}(\omega_1, t)$ is quite lengthy. However, by assuming that $|\omega_0| \gg |\omega_Q| \gg |\omega_1|$, it can be effectively reduced to a form corresponding to all ideal selective rotations as defined in Appendix A. This can be shown by expanding the elements of the matrix $\mathcal{U}(\omega_1, t)$ in a power series of the parameter $\epsilon = |\omega_1|/|\omega_Q|$ and, finally, keeping only the first term of this expansion.

For example, if the pulse is resonant with the central transition, then the evolution operator $\mathcal{U}(\omega_1, t)$ can be approximated by

$$\mathcal{U}_{12}(\omega_1, t_p) = \begin{bmatrix} \delta^* & 0 & 0 & 0 \\ 0 & \delta\cos(\omega_1 t_p) & -i\delta\sin(\omega_1 t_p) & 0 \\ 0 & -i\delta\sin(\omega_1 t_p) & \delta\cos(\omega_1 t_p) & 0 \\ 0 & 0 & 0 & \delta^* \end{bmatrix}, \quad (15)$$

where $\delta = \exp(i\omega_Q t_p)$. Note that $\mathcal{U}_{12}(\omega_1, t)$ reduces to the perfect selective rotation $\mathcal{X}_{12}(\theta) = R_{12}^{(X)}(\theta)$, with $\theta = 2\omega_1 t_p$, if the pulse duration is chosen such that $\omega_Q t_p$ is a multiple of 2π. Analogously, other rotations $R_{mn}^{(i)}(\theta)$, given by Eq. (A4), can be implemented for $i = X, Y, Z$ and $m, n = 0, \ldots, 3$ with $m \neq n$.

III. IMPLEMENTING GATES IN SPIN-3/2 SYSTEM

Here we discuss how to implement single- and two-qubit gates in systems with spin-3/2. This can enable formally simple implementations of arbitrary multiqubit quantum algorithms by applying sequences of NMR pulses in multilevel spin systems. We focus on various NMR QST methods for a system with spin-3/2 nuclei but our analysis can be easily generalized for larger spins.

Due to the Zeeman and quadrupolar interactions (shown in Fig. 1), a spin-3/2 system is described in an external magnetic field by a nonequidistant four-level energy spectrum. Thus, this system can be referred to as a *quartit* (also called ququart or four-level qudit). The basic set of eigenfunctions of the system can be described with the states $|mn\rangle \equiv |m\rangle_A|n\rangle_B$ of two logical (or virtual) qubits A and B corresponding to an ensemble of identical spin-1/2 pairs:

$$\begin{aligned} \left|\tfrac{3}{2}, \tfrac{3}{2}\right\rangle &\equiv |0\rangle \equiv |00\rangle, & \left|\tfrac{3}{2}, -\tfrac{1}{2}\right\rangle &\equiv |2\rangle \equiv |10\rangle, \\ \left|\tfrac{3}{2}, \tfrac{1}{2}\right\rangle &\equiv |1\rangle \equiv |01\rangle, & \left|\tfrac{3}{2}, -\tfrac{3}{2}\right\rangle &\equiv |3\rangle \equiv |11\rangle. \end{aligned} \quad (16)$$

A pure state of a quartit can be written in this basis states as

$$|\psi\rangle = c_0|0\rangle + c_1|1\rangle + c_2|2\rangle + c_3|3\rangle \quad (17)$$

in terms of the normalized complex amplitudes c_i, so an arbitrary mixed state of a quartit is described by a density matrix $\rho = [\rho_{nm}]_{4\times4}$.

Our discussion in this section is based on a fundamental theorem in quantum information according to which any quantum gate can be constructed from single-qubit rotations and any nontrivial two-qubit gate, e.g., the CNOT gate [1]. In a quartit, rotations of a virtual qubit A and B, denoted, respectively, by $R^A(\theta)$ and $R^B(\theta)$, can be implemented by the application of two pulses:

$$R^A(\theta) = R_{02}(\theta)R_{13}(\theta), \quad R^B(\theta) = R_{01}(\theta)R_{23}(\theta), \quad (18)$$

where $R_{mn}(\theta)$ (with $R = X, Y, Z$) is a selective rotation resonant with a transition between levels $|m\rangle$ and $|n\rangle$ as defined in Appendix A (see also Fig. 2).

Note that realizations of *single* virtual qubit gates in a qudit are more complicated than those for real qubits. In contrast to those, usually *two* virtual qubit gates can be realized much simply, e.g., a CNOT-like gate can be implemented by applying

a *single* π pulse, e.g.,

$$S_{23} \equiv U'_{\mathrm{CNOT}} = \begin{bmatrix} 1 & 0 & 0 & 0 \\ 0 & 1 & 0 & 0 \\ 0 & 0 & 0 & -1 \\ 0 & 0 & 1 & 0 \end{bmatrix} = \mathcal{Y}_{23}(\pi). \quad (19)$$

Similarly, a SWAP-like gate can also be implemented easily by a *single* π pulse:

$$S_{12} \equiv U'_{\mathrm{SWAP}} = \begin{bmatrix} 1 & 0 & 0 & 0 \\ 0 & 0 & -1 & 0 \\ 0 & 1 & 0 & 0 \\ 0 & 0 & 0 & 1 \end{bmatrix} = \mathcal{Y}_{12}(\pi). \quad (20)$$

The above CNOT-like and SWAP-like gates can be related to the standard CNOT and SWAP gates as follows:

$$U_{\mathrm{CNOT}} = D U'_{\mathrm{CNOT}}, \quad U_{\mathrm{SWAP}} = U'_{\mathrm{SWAP}} D, \quad (21)$$

where $D = \mathrm{diag}([1, 1, -1, 1])$. One can define a SWAP-like gate S_{nm} between any levels $|n\rangle$ and $|m\rangle$ in a quartit, simply as

$$S_{nm} = \mathcal{Y}_{nm}(\pi), \quad (22)$$

which in special cases reduce to Eqs. (19) and (20).

It is worth noting that any unitary operator that can create entanglement between a pair of qubits (or virtual qubits) is universal. Thus, the standard SWAP gate U_{SWAP} is not universal, as its entangling power is zero. In contrast to this gate, the SWAP-like gate U'_{SWAP} *is universal*, as it can entangle qubits.

IV. PRINCIPLES OF M_z-BASED QST

NMR quantum state tomography is a method for the complete reconstruction of a given density matrix ρ in a series of NMR measurements. In general, to completely reconstruct a density matrix ρ for a quartit or two qubits, we need to determine 16 real parameters. Note that if the efficiency of a given detection system is known then the 16th element can typically be found from the normalization condition. Single-NMR readout can only give some elements of ρ: either diagonal (in case of M_z detection) or off-diagonal elements (for M_{xy} detection), as discussed in Appendix B. The remaining matrix elements of the original density matrix ρ can be obtained by rotating it through properly chosen rotational operations $R^{(k)}$, which change ρ as follows:

$$\rho^{(k)} \equiv R^{(k)} \rho (R^{(k)})^\dagger. \quad (23)$$

These operations are performed before NMR readout measurements. Thus, the reconstruction of a given density matrix is possible by transforming ρ through various rotations $R^{(k)}$ in such a way that all the elements of ρ go over into measurable ones in a given detection method.

In the standard NMR M_{xy} detection, one can directly determine some of the off-diagonal elements of the density matrix. In contrast to the M_{xy} detection, one directly determines only diagonal elements in the M_z detection. It is worth noting that the spectrum of a spin-3/2 system obtained via the M_z detection contains less information than the spectra obtained by the M_{xy} detection as discussed in Appendix B: The M_{xy} detection of a spin-3/2 system yields six real values, which correspond to three peaks of real and those of imaginary parts

of the spectrum. Note that the M_{xy} detection of a coupled two spin-1/2 system can yield even more values if one could detect signals from ensembles of two different spins simultaneously.

Tomography based on the measurements of the M_z and M_{xy} magnetizations of spin-3/2 systems has been performed in experiments reported in Refs. [16] and [17], respectively.

A. An implementation of M_z detection in a nanometer-scale device

Here we briefly describe an implementation of the NMR detection of the longitudinal magnetization of a small ensemble of quadrupolar spins-3/2, which is beyond the detection limits of conventional NMR techniques [33,41–44,46].

This NMR detection was developed and applied in Refs. [42] to an on-chip semiconductor device based on a quantum-well structure shown in Fig. 3. This nanometer-scale device is composed of a monolithic GaAs quantum well integrated with a point contact channel and an antenna gate, where an RF field can be locally applied. The GaAs layer effectively forms a two-dimensional electron gas. The point-contact channel is composed of isotopes ^{69}Ga, ^{71}Ga, and ^{75}As having total ground-state spin $I = 3/2$. The nuclear spins in the channel can be selectively polarized by flowing current, while the spins in the other regions are kept in thermal equilibrium. These interactions between electron and nuclear spins are enhanced when an external static magnetic field B_0 is applied to set the system at the spin phase transition of the Landau level filling factor 2/3 [53]. The polarization is followed by RF pulses applied through the antenna gate, which enable manipulation of the nuclear spins. This coherent manipulation results in oscillations of the resistance of the point-contact channel, which are directly related to the oscillations in the longitudinal magnetization M_z. Reference [42] observed clear oscillations reflecting all possible transitions between the four nuclear-spin states (see Fig. 2) of each nuclide (^{69}Ga, ^{71}Ga, and ^{75}As). This novel device, exhibiting extremely low decoherence [42,44], opens new perspectives to study characteristics of nuclear spins in nanoscale semiconductors but also to precisely control nuclear-spin states. The arbitrary control of the superposition of the four spin-3/2 states enables the implementation of two-qubit coherent operations [33,43]. Thus, the device offers new possibilities to perform single- and two-qubit quantum gates or even to test simple quantum-information processing algorithms. A fabrication of analogous device based on InAs and InSb [54], instead of GaAs, where the isotopes ^{113}In and ^{115}In have spin $I = 9/2$ (a 10-level qudit) and the isotope ^{123}Sb has spin $I = 7/2$ (an 8-level qudit), would enable the implementation of three-qubit quantum gates and algorithms. But it must be admitted that the devices are not easily scalable for much higher number of virtual and/or real qubits.

The initialization of the described device is relatively easy. We can realize the effective pure state $|3\rangle$ by using current-induced nuclear spin polarization with randomizing pulses of ω_{01} and ω_{12}. Once the state $|3\rangle$ is realized, it is transferred to $|0\rangle$, $|1\rangle$, and $|2\rangle$ by applying a respective π pulse as described by us in Refs. [33,43].

The estimated polarization of the nuclear spins is quite high. Therefore, obtaining initial states with high purity should be
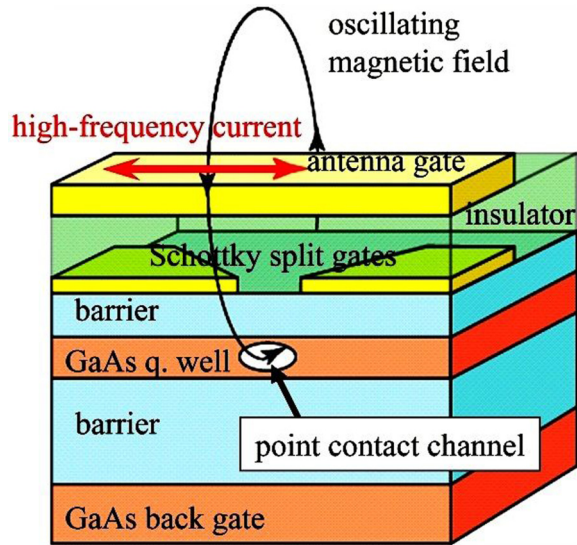
FIG. 3. (Color online) Schematic diagram of the implementation of a coherently and selectively controllable solid-state system with nuclear spins-3/2 for quantum information processing and quantum tomography. This is an on-chip monolithic semiconductor device integrated with a point-contact channel, fabricated by Yusa *et al.* [42]. The point-contact channel (indicated with an arrow), as defined by a pair of Schottky split gates, is composed of a small ensemble of nuclear quadrupolar spins-3/2 of isotopes ^{69}Ga, ^{71}Ga, and ^{75}As. The nuclear spins in this device can exhibit extremely long decoherence times (a few milliseconds). The antenna gate, which is insulated from the Schottky gates, can locally irradiate the channel with an RF field. The ensemble of spins-3/2 in the channel can be selectively and coherently polarized and controlled by NMR techniques. The resistance of the channel changes after an RF pulse, which directly corresponds to the change of the longitudinal magnetization M_z induced by the change in the population of nuclear-spin states. Thus, the discussed tomographic methods, which are based on the detection of the longitudinal magnetization of nuclear spins, can be effectively implemented in such devices. This device is based on a quantum-well GaAs structure, but other semiconductors can also be used. For example, by using the semiconductor $FeSb_2$, instead of GaAs, the coherent control of nuclear quadrupolar spins-7/2 for the isotope ^{123}Sb would enable quantum information processing with a quoctit (eight-level qudit) corresponding to three virtual qubits. This figure is based on Fig. 1(b) in Ref. [42].

practically quite simple—at least to start with the pseudopure states $|0\rangle$ or $|4\rangle$.

There are many different possibilities to measure spectra. The following is the simplest example applied in experiments described in Ref. [33]. After the preparation of a desired state, we apply a pulse with a duration corresponding to a π pulse and measure how a resistance changes as a function of frequency. In case of the constant pulse-current amplitude, the length of the π pulse changes $1/\sqrt{3} : 1/\sqrt{4} : 1/\sqrt{3}$ for ω_{01}, ω_{12}, and ω_{23}, respectively. (These differences can be ignored in a simple experiment.) From this spectrum, we can estimate a population difference between neighboring states, i.e., $\rho_{11} - \rho_{00}$, $\rho_{22} - \rho_{11}$, and $\rho_{33} - \rho_{22}$ (see Sec. VI B). Another experimental observation approach will be described in Sec. VI C.

V. LINEAR RECONSTRUCTION AND THE ERROR ROBUSTNESS

Various numerical procedures for reconstructing an unknown density matrix ρ from experimental data have been developed (see, e.g., Refs. [2,3] and references therein).

The simplest and most intuitive QST is based on the inversion of a linear system,

$$Ax = b, \tag{24}$$

where the real vector $x = \mathrm{vec}(\rho)$ corresponds to the state ρ to be reconstructed. This vector can be defined in various ways. Here, for a quartit state, we define x as

$$x = \mathrm{vec}(\rho) = [\rho_{00}, \mathrm{Re}\,\rho_{01}, \mathrm{Im}\,\rho_{01}, \mathrm{Re}\,\rho_{02}, \mathrm{Im}\,\rho_{02}, \dots, \rho_{33}]^T, \tag{25}$$

where ρ_{ij}, for $i \leqslant j$, are only included. Thus, a density matrix ρ can be expressed via the elements of the vector x as follows:

$$\rho = \begin{bmatrix} x_1 & x_2 + ix_3 & x_4 + ix_5 & x_6 + ix_7 \\ x_2 - ix_3 & x_8 & x_9 + ix_{10} & x_{11} + ix_{12} \\ x_4 - ix_5 & x_9 - ix_{10} & x_{13} & x_{14} + ix_{15} \\ x_6 - ix_7 & x_{11} - ix_{12} & x_{14} - ix_{15} & x_{16} \end{bmatrix}. \tag{26}$$

Moreover, in Eq. (24), b is the *observation vector*, which contains the measured data, and A is the *coefficient matrix*, which is also referred to as the rotation matrix or the data matrix in a more mathematical context. Thus, the element A_{ji} is the coefficient of x_i in the jth equation ($j = 1, \dots, N_{\mathrm{eqs}}$) for a chosen measurement rotation. In our context, the observation vector b_j corresponds to the integrated area of the NMR spectra. The number N_{eqs} of equations is given by $N_r \times N_{\mathrm{vals}}$, assuming N_r readouts (for a given measurement), where each of them yields N_{vals} values corresponding, e.g., to the number of peaks of an NMR spectrum (including both real and imaginary parts). Usually, an extra equation is added for the normalization condition, $\mathrm{Tr}\rho = 1$. Thus, for a quartit, the observation vector has N_{eqs} elements and the coefficient matrix A is of dimensions $N_{\mathrm{eqs}} \times 16$.

Usually, there are more equations than unknowns. Such *overdetermined* problems can be solved as

$$Cx = \tilde{b}, \tag{27}$$

where $C \equiv [C_{ij}]_{16 \times 16} = A^\dagger A$ and $\tilde{b} \equiv [\tilde{b}_j]_{16 \times 1} = A^\dagger b$. Equation (27) results from the standard least-squares-fitting analysis based on the minimalization of $\chi^2 = ||Ax - b||^2$. Thus, one can easily calculate the solution $x = C^{-1}\tilde{b}$ and, finally, reconstruct the sought density matrix as

$$\rho = \mathrm{vec}^{-1}(x) = \mathrm{vec}^{-1}(C^{-1}\tilde{b}), \tag{28}$$

as the inverse of Eq. (25).

Dozens of different linear-inversion-based QST protocols have been proposed and applied (see, e.g., Refs. [2,3] and references citing those). Then the question arises: Which of them are preferable for certain goals and tasks?

As an indicator of the quality of a linear-inversion-based QST method, or, more precisely, its error robustness (or error sensitivity), one can apply the so-called *condition number* defined as [55–57]:

$$\mathrm{cond}_{\alpha,\beta}(C) = ||C||_{\alpha,\beta}\,||C^{-1}||_{\beta,\alpha} \geqslant 1, \tag{29}$$

where C is a nonsingular square matrix and the convention is used that $\mathrm{cond}_{\alpha,\beta}(C) = +\infty$ for a singular matrix C. Moreover, $\|\cdot\|_{\alpha,\beta}$ denotes the subordinate matrix norm, which can be defined via the vector norms: $\|C\|_{\alpha,\beta} = \max_{x \neq 0} \|Cx\|_{\beta}/\|x\|_{\alpha}$. Clearly, the condition numbers depend on the applied norm. Here, we apply the spectral norm only.

The spectral norm (also refereed to as the 2-norm) is given by the largest singular value of C, i.e, $\|C\|_2 \equiv \|C\|_{2,2} = \max[\mathrm{svd}(C)] \equiv \sigma_{\max}(C)$, where the function $\mathrm{svd}(C)$ gives the singular values of C. Then this condition number is simply given by

$$\kappa(C) \equiv \mathrm{cond}_{22}(C) = \frac{\sigma_{\max}(C)}{\sigma_{\min}(C)}, \tag{30}$$

where we have used $\|C^{-1}\|_2 = \max[\mathrm{svd}(C^{-1})] = \{\min[\mathrm{svd}(C)]\}^{-1} \equiv \sigma_{\min}^{-1}(C)$. There are various geometrical, algebraic, and physical interpretations of condition numbers (see Ref. [8] and references therein, in addition to Refs. [55–58]). In particular, according to the Gastinel-Kahan theorem, the inverse of a condition number corresponds to the relative distance of a nonsingular square matrix C to the set of singular matrices. Another, more physical, interpretation can be given as follows [55]: Let us assume errors $\delta\tilde{b}$ in the observation vector $\tilde{b}$, which cause errors δx in the reconstructed vector x:

$$C(x + \delta x) = \tilde{b} + \delta\tilde{b}, \tag{31}$$

then the following inequalities hold:

$$\frac{1}{\mathrm{cond}_{\alpha,\beta}(C)} \frac{||\delta\tilde{b}||}{||\tilde{b}||} \leqslant \frac{||\delta x||}{||x||} \leqslant \mathrm{cond}_{\alpha,\beta}(C) \frac{||\delta\tilde{b}||}{||\tilde{b}||}. \tag{32}$$

It is clear that when a condition number $\mathrm{cond}_{\alpha,\beta}(C) \approx 1$, then small relative changes in the observation vector $\tilde{b}$ cause equally small relative changes in the reconstructed state x. This interpretation can be generalized to include also errors δC in the coefficient matrix C.

Thus, by applying this general theorem, given in Eq. (32), to QST, we can conclude that if $\mathrm{cond}_{\alpha,\beta}(C)$ is small (large), then the coefficient matrix C and the corresponding QST method are called *well-conditioned* (*ill-conditioned*), which means that the method is robust (sensitive) to errors in the observation vector $\tilde{b}$. For ill-conditioned QST, even a minor error in $\tilde{b}$ can cause a large error in x. Some instructive numerical examples of ill-conditioned problems are given in Refs. [8,55].

Condition numbers were applied to estimate the quality of optical tomographic reconstructions in, e.g., Refs. [8,59]. A condition number was also calculated for the NMR tomography of two qubits (two spins-1/2) [60]. However, to our knowledge, these parameters have not been applied yet to analyze the quality of QST of any *qudit* systems. More importantly, none of the previous NMR tomographic methods exhibits the optimum robustness against errors as described by a condition number equal or almost equal to 1. Below we propose a few NMR QST protocols and compare their error robustness based on the condition numbers to show that some of our methods are optimal.

Note that the smallest singular value (or, equivalently, eigenvalue) $\sigma_{\min}(C) = \min[\mathrm{svd}(C)] = \|C^{-1}\|_2$ of C is also sometimes used as an error-robustness parameter. This ap-

proach was applied in the analysis of an NMR QST method in, e.g., Ref. [61]. In comparison to $\sigma_{\min}(C)$, the condition numbers are much better parameters of the error robustness as discussed in, e.g., Ref. [8].

VI. OBSERVATION APPROACHES

Here we specify three observation approaches based on the M_z detection to be studied in detail in the next sections.

A. Theoretical approach

In an ideal M_z detection, one can directly access all the diagonal elements

$$b_n^{(k)} = \rho_{nn}^{(k)} \tag{33}$$

of any rotated density matrix $\rho^{(k)} \equiv R^{(k)} \rho \left(R^{(k)}\right)^\dagger$ for $k = 1, \ldots, N_r$, where N_r is the number of readouts (operations or sets of rotations). We refer to this purely theoretical method as the *theoretical approach*.

B. Ideal experimental approach

In a more realistic observation approach, the information is gathered from the M_z spectra, where one can roughly estimate the population differences ($\rho_{11} - \rho_{00}$, $\rho_{22} - \rho_{11}$, and $\rho_{33} - \rho_{22}$) from the amplitude of the signals by integrating the area of the peaks centered at ω_{01}, ω_{12}, and ω_{23}, respectively. Thus, on including the normalization condition, we have the following set of equations:

$$b_n^{(k)} = \rho_{n+1,n+1}^{(k)} - \rho_{nn}^{(k)} = \mathrm{Tr}\left(I_z^{(n+1,n)}\rho^{(k)}\right), \quad 1 = \mathrm{Tr}\rho^{(k)}, \tag{34}$$

for each rotated density matrix $\rho^{(k)}$, where $I_z^{(n+1,n)} = |n+1\rangle\langle n+1| - |n\rangle\langle n|$ is the fictitious spin-1/2 operator for general spin. Note that $b_n^{(k)}$ can be rescaled as $\bar{b}_n^{(k)}\mathcal{N}$, where the constant $\mathcal{N}$ is usually chosen so the thermal equilibrium magnetization vector is equal to a unit vector along the z axis [51]. By referring to the ideal experimental approach, we mean that based on Eq. (34).

Alternatively, the measured resistance in experiments performed in, e.g., Refs. [33,42,43], can be proportional to the longitudinal magnetization $M_z \propto \mathrm{Tr}[\rho I_z]$ defined in terms of the total angular momentum operator $I_z = \mathrm{diag}([\frac{3}{2}, \frac{1}{2}, -\frac{1}{2}, -\frac{3}{2}])$ for spin $I = 3/2$:

$$M_z^{(k)} \propto \mathrm{Tr}[\rho^{(k)} I_z] = \tfrac{1}{2}\left(3\rho_{00}^{(k)} + \rho_{11}^{(k)} - \rho_{22}^{(k)} - 3\rho_{33}^{(k)}\right). \tag{35}$$

However, instead of studying this approach based on Eq. (35), we apply a more practical observation method based on the cyclically ordered phase sequence (CYCLOPS) technique.

C. Nonideal experimental approach using CYCLOPS

Here we study a practical measurement method by applying the standard CYCLOPS to a $\pi/20$ reading pulse and receiver [62]. This method was used in, e.g., the experiment on QST for quadrupolar nuclei of a liquid crystal by Bonk *et al.* [16]. In this observation approach, the NMR spectra were obtained from free induction decay (FID) averaged over each phase $(x, -y, -x, y)$. This enables the suppression of receiver

imperfections and, thus, the cancellation of artifacts from the NMR spectra. The intensities $b_n^{(k)}$ of the three ($n = 1,2,3$) peaks of the averaged NMR spectrum for the rotated deviation matrices

$$\Delta\rho^{(k)} \equiv \rho^{(k)} - \tfrac{1}{4}\mathcal{I}, \quad \text{for } k = 1,\ldots,N_r, \quad (36)$$

together with the normalization conditions are described by the following set of equations for, e.g., the quartit:

$$\left[b_1^{(k)},b_2^{(k)},b_3^{(k)}\right]^T = V\,\mathrm{diag}(\Delta\rho^{(k)}), \quad 0 = \mathrm{Tr}(\Delta\rho^{(k)}), \quad (37)$$

where [16]:

$$V = \begin{bmatrix} \sqrt{3}e_{11}e_{12} & -\sqrt{3}e_{12}e_{22} & -\sqrt{3}e_{23}e_{13} & -\sqrt{3}e_{13}e_{14} \\ 2e_{13}e_{12} & 2e_{22}e_{23} & -2e_{23}e_{22} & -2e_{13}e_{12} \\ \sqrt{3}e_{13}e_{14} & \sqrt{3}e_{13}e_{23} & \sqrt{3}e_{12}e_{22} & -\sqrt{3}e_{11}e_{12} \end{bmatrix}. \quad (38)$$

The nth NMR peak corresponds to the transition between levels $|n-1\rangle$ and $|n\rangle$. Above, $\mathrm{diag}(\Delta\rho^{(k)})$ denotes a column vector of the diagonal elements of $\Delta\rho^{(k)}$. The coefficients e_{ij} are the absolute values of the $\pi/20$ hard-reading pulse given by:

$$[e_{ij}] = \frac{1}{4}\begin{bmatrix} c_{31} & s_{zz} & c_{z,-z} & s_{3,-1} \\ s_{zz} & c_{13} & s_{-1,3} & c_{z,-z} \\ c_{z,-z} & s_{-1,3} & c_{13} & s_{zz} \\ s_{3,-1} & c_{z,-z} & s_{zz} & c_{31} \end{bmatrix}, \quad (39)$$

where $c_{xy} = x\cos(\frac{\pi}{40}) + y\cos(\frac{3\pi}{40})$, $s_{xy} = x\sin(\frac{\pi}{40}) + y\sin(\frac{3\pi}{40})$, and $z = \sqrt{3}$. It seems that this method results in the coefficient matrices, which completely differ from those obtained in the ideal experimental approach. However, we will show that they are practically very similar.

VII. OPTIMAL RECONSTRUCTION OF THE DIAGONAL ELEMENTS OF ρ

Here we analyze the error robustness based on the condition number κ for the reconstruction of only diagonal terms ρ_{nn} of a quartit density matrix ρ for the three observation approaches using various sets of rotations.

A. Theoretical approach

In the theoretical observation approach, we assume a direct access to all the diagonal terms of ρ:

$$\begin{aligned} b_1^{(1)} &= \rho_{00} \equiv x_1, & b_2^{(1)} &= \rho_{11} \equiv x_8, \\ b_3^{(1)} &= \rho_{22} \equiv x_{13}, & b_4^{(1)} &= \rho_{33} \equiv x_{16}, \end{aligned} \quad (40)$$

where $\rho = \rho^{(1)}$. This implies that this partial tomography is perfectly robust against errors, as described by the condition number $\kappa = 1$. Obviously, this robustness does not guarantee that complete tomographic methods can also be perfectly robust against errors.

B. Ideal experimental approach

The set of equations (34) directly leads to the coefficient matrices, which in general differ from those obtained by a direct measurement of all the diagonal elements of ρ.

Nevertheless, from Eq. (34), one can easily determine all the diagonal elements $\rho^{(k)}$, e.g., as follows:

$$\begin{aligned} \rho_{00}^{(k)} &= \tfrac{1}{4} - \tfrac{1}{4}\big(3b_1^{(k)} + 2b_2^{(k)} + b_3^{(k)}\big), \\ \rho_{11}^{(k)} &= \tfrac{1}{4} + \tfrac{1}{4}\big(b_1^{(k)} - 2b_2^{(k)} - b_3^{(k)}\big), \\ \rho_{22}^{(k)} &= \tfrac{1}{4} + \tfrac{1}{4}\big(b_1^{(k)} + 2b_2^{(k)} - b_3^{(k)}\big), \\ \rho_{33}^{(k)} &= \tfrac{1}{4} + \tfrac{1}{4}\big(b_1^{(k)} + 2b_2^{(k)} + 3b_3^{(k)}\big). \end{aligned} \quad (41)$$

We can rewrite this problem in a matrix form, given by Eq. (24), with its solution $x = (A_{\mathrm{diag}}^{\mathrm{temp1}})^{-1}b$, where

$$A_{\mathrm{diag}}^{\mathrm{temp1}} = \begin{bmatrix} -1 & 1 & 0 & 0 \\ 0 & -1 & 1 & 0 \\ 0 & 0 & -1 & 1 \\ 1 & 1 & 1 & 1 \end{bmatrix}, \quad (42)$$

$$x = [\rho_{00},\rho_{11},\rho_{22},\rho_{33}]^T, \quad (43)$$

$$b = \left[b_1^{(1)},b_2^{(1)},b_3^{(1)},1\right]^T, \quad (44)$$

where, as usual, $b_n^{(1)}$ corresponds to the nth peak resulting from the transition between the levels $|n-1\rangle$ and $|n\rangle$ in the original matrix $\rho = \rho^{(1)}$. The condition number reads $\kappa(A^T A) = 6.83$ for $A \equiv A_{\mathrm{diag}}^{\mathrm{temp1}}$. Thus, this direct application of the ideal experimental observation method to reconstruct *only* the diagonal terms of ρ for a quartit can magnify the relative error in the observation vector b by almost one order of magnitude.

Nevertheless, in the following, we show how to achieve $\kappa(A^T A) = 1$, even if the diagonal matrix elements are not directly measured. It is worth noting that the condition number $\kappa(A^T A)$ can also be equal to 1 for analogous M_z-based QST of the diagonal elements of a density matrix for two spatially separated qubits. This is because the diagonal matrix elements can be directly measured, so no reconstruction of these elements is required.

Note that this coefficient matrix $A_{\mathrm{diag}}^{\mathrm{temp1}}$ is unbalanced, which implies that some elements of ρ are measured more often than others. Specifically, there are only two nonzero elements in the first and last columns of $A_{\mathrm{diag}}^{\mathrm{temp1}}$ (corresponding to ρ_{00} and ρ_{33}) and three nonzero elements in the other columns of A (corresponding to ρ_{11} and ρ_{22}). To overcome this problem, let us apply the pulse $S_{13} \equiv \mathcal{Y}_{13}(\pi)$, which corresponds to the SWAP-like gate. Then we measure only the first peak (corresponding to the transition $|0\rangle \leftrightarrow |1\rangle$) of the rotated density matrix $S_{13}\rho S_{13}^\dagger$. Thus, by adding this equation to $A_{\mathrm{diag}}^{\mathrm{temp1}}$, one obtains

$$A_{\mathrm{diag}}^{\mathrm{temp2}} = \left[A_{\mathrm{diag}}^{\mathrm{temp1}}; (-1,0,0,1)\right]. \quad (45)$$

Then the condition number becomes $\kappa(A^T A) = 2$ for $A = A_{\mathrm{diag}}^{\mathrm{temp2}}$, which is much smaller than that for $A = A_{\mathrm{diag}}^{\mathrm{temp1}}$. One can then obtain a more balanced coefficient matrix $A_{\mathrm{diag}}^{\mathrm{opt}}$ by adding two equations to $A_{\mathrm{diag}}^{\mathrm{temp2}}$, which correspond to the first peak of the rotated density matrices $S_{12}\rho S_{12}^\dagger$ and $S_{03}\rho S_{03}^\dagger$.
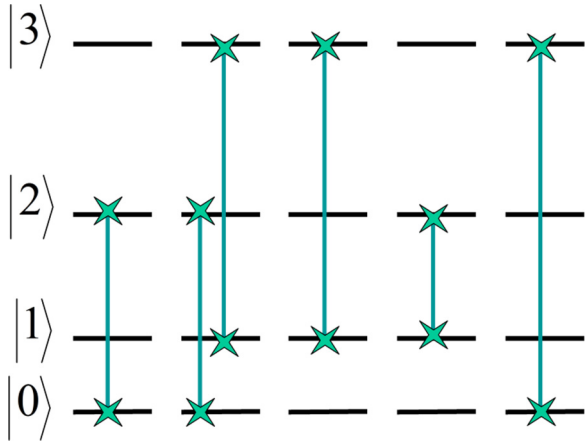
FIG. 4. (Color online) Set of rotations $R_{\text{diag}}^{\text{opt1}}$, given in Eq. (47), which enables the optimal reconstruction of all the diagonal elements of ρ, by measuring only the first peak of the M_z spectra, i.e., the peak corresponding to the transition $|0\rangle \leftrightarrow |1\rangle$. The operation marked by $\times\!-\!\times$ denotes the SWAP-like operation $S_{nm} \equiv \mathcal{Y}_{nm}(\pi)$ between the levels $|n\rangle$ and $|m\rangle$. Reading pulses (which are not shown here) are applied only after applying these SWAP-like gates. The set $R_{\text{diag}}^{\text{opt1}}$ corresponds to the coefficient matrix $A \equiv A_{\text{diag}}^{\text{opt1}}$, given in Eq. (46), yielding the smallest condition number $\kappa(A^T A) = 1$. Note that the last row in A corresponds to the normalization condition, while the first row corresponds to applying a reading pulse without the SWAP. For brevity, this trivial case corresponding to the identity operation is not presented here.

Thus, we have

$$A_{\text{diag}}^{\text{opt1}} = \begin{pmatrix} -1 & 1 & 0 & 0 \\ 0 & 1 & -1 & 0 \\ 0 & 0 & -1 & 1 \\ -1 & 0 & 0 & 1 \\ -1 & 0 & 1 & 0 \\ 0 & 1 & 0 & -1 \\ s & s & s & s \end{pmatrix}. \tag{46}$$

Note that we have multiplied the second row in Eq. (42) by the factor (-1) to obtain Eq. (46), which enables us to slightly simplify the following Eq. (47). This operation does not affect the corresponding condition numbers. As usual, the last row (equation) in Eq. (46) corresponds to the normalization condition, where s is the scaling factor, which is set here as $s = 1$. Then we find that $C_{\text{diag}}^{\text{opt}} = (A_{\text{diag}}^{\text{opt1}})^{\dagger} A_{\text{diag}}^{\text{opt1}} = 4I_4$, where I_4 is the four-dimensional identity operator. In general, this factor s determines the contribution of the last equation to the whole set $Ax = b$ of equations and can be chosen such that κ is minimized.

Thus, we have shown that the condition number $\kappa(C_{\text{diag}}^{\text{opt}}) = 1$ indicates the optimality of the coefficient matrix $A_{\text{diag}}^{\text{opt}}$ for the ideal experimental observation approach. This matrix $A_{\text{diag}}^{\text{opt}}$ can be obtained from the following set of rotations:

$$R_{\text{diag}}^{\text{opt1}} = [I, S_{02}, S_{13}S_{02}, S_{13}, S_{12}, S_{03}], \tag{47}$$

as shown in Fig. 4, using the SWAP-like gates $S_{nm} \equiv \mathcal{Y}_{nm}(\pi)$. Here we assume that only the first peak is measured, while the other two peaks are ignored, in the M_z spectra of the rotated

density matrices $\rho^{(k)} = R^{(k)}\rho\,(R^{(k)})^{\dagger}$ for all the rotations $R^{(k)}$ in Eq. (47).

Alternatively, we can swap the elements ρ_{nn} in such a way that only the central peak, corresponding to $|1\rangle \leftrightarrow |2\rangle$, is measured. Namely, one can use the following set of rotations:

$$R_{\text{diag}}^{\text{opt2}} = [I, S_{02}, S_{13}, S_{01}S_{23}, S_{01}, S_{23}], \tag{48}$$

as shown in Fig. 5, which leads to the following coefficient matrix:

$$A_{\text{diag}}^{\text{opt2}} = \begin{pmatrix} 0 & -1 & 1 & 0 \\ 1 & -1 & 0 & 0 \\ 0 & 0 & 1 & -1 \\ -1 & 0 & 0 & 1 \\ -1 & 0 & 1 & 0 \\ 0 & -1 & 0 & 1 \\ s & s & s & s \end{pmatrix}, \tag{49}$$

where the last row corresponds, as usual, to the normalization condition. By setting $s = 1$, one finds that $C_{\text{diag}}^{\text{opt}} = (A_{\text{diag}}^{\text{opt2}})^{\dagger} A_{\text{diag}}^{\text{opt2}} = 4I_4$, the same as for $(A_{\text{diag}}^{\text{opt1}})^{\dagger} A_{\text{diag}}^{\text{opt1}}$. This property holds since $A_{\text{diag}}^{\text{opt1}}$ and $A_{\text{diag}}^{\text{opt2}}$ differ only in the order of their rows and in the opposite sign of all the elements of some of their rows. So these coefficient matrices can be considered equivalent,

$$A_{\text{diag}}^{\text{opt1}} \cong A_{\text{diag}}^{\text{opt2}}. \tag{50}$$

Moreover, the two-photon rotations, given in Eq. (48), can be replaced by single-photon transitions, e.g., S_{02} can be replaced by $S_{01}S_{12}$, and S_{13} by $S_{12}S_{23}S_{12}$, as will be described in general terms in Sec. X. This might be an advantage from the experimental point of view.

It is worth noting that the state vector x is defined as in Eq. (43) for both methods, based on the rotations $R_{\text{diag}}^{\text{opt1}}$ and $R_{\text{diag}}^{\text{opt2}}$. However, the observation vectors b are defined as follows: (i) For the rotations $R_{\text{diag}}^{\text{opt1}}$, one measures

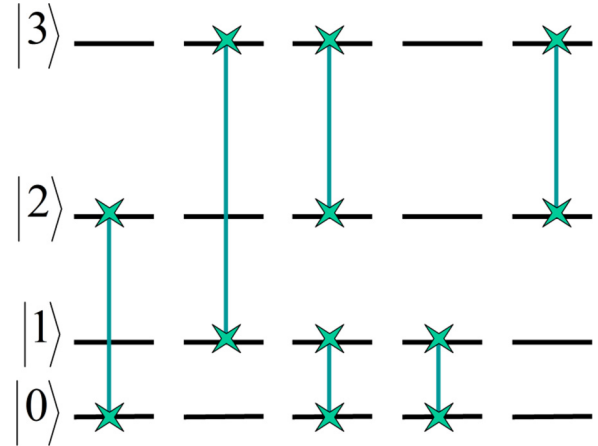$$b = \left[b_1^{(1)}, b_1^{(2)}, \ldots, b_1^{(6)}, s\right]^T, \tag{51}$$

FIG. 5. (Color online) Set of rotations $R_{\text{diag}}^{\text{opt2}}$, given in Eq. (48). Same as in Fig. 4, but the coefficient matrix $A_{\text{diag}}^{\text{opt2}}$ corresponds to measuring only the central peak of the M_z spectra, i.e., that corresponding to the transition $|1\rangle \leftrightarrow |2\rangle$.

where $b_1^{(k)}$ corresponds to the first peak obtained for the rotated density matrix $\rho^{(k)} = R_{\mathrm{diag},k}^{\mathrm{opt1}} \rho\, (R_{\mathrm{diag},k}^{\mathrm{opt1}})^\dagger$. (ii) For the rotations $R_{\mathrm{diag}}^{\mathrm{opt2}}$, the observation vector reads

$$b = \left[b_2^{(1)}, b_2^{(2)}, \ldots, b_2^{(6)}, s\right]^T, \tag{52}$$

where $b_2^{(k)}$ corresponds to the second peak obtained for $\rho^{(k)} = R_{\mathrm{diag},k}^{\mathrm{opt2}} \rho\, (R_{\mathrm{diag},k}^{\mathrm{opt2}})^\dagger$.

C. Nonideal experimental approach using CYCLOPS

The set of Eqs. (37) can be rewritten in the matrix form $Ax = b$, where

$$A_{\mathrm{diag}}^{\mathrm{temp3}} = [V; (s,s,s,s)], \tag{53}$$

$$x = \left[\rho_{00} - \tfrac{1}{4}, \rho_{11} - \tfrac{1}{4}, \rho_{22} - \tfrac{1}{4}, \rho_{33} - \tfrac{1}{4}\right]^T, \tag{54}$$

$$b = \left[b_1^{(1)}, b_2^{(1)}, b_3^{(1)}, 0\right]^T. \tag{55}$$

Then we find the condition number to be $\kappa(A^T A) = 98.46$ if $A = A_{\mathrm{diag}}^{\mathrm{temp3}}$ and $s = 1$. It means that the determination of all the diagonal terms of ρ for a quartit using the standard CYCLOPS method can be relatively sensitive to errors. Indeed, the relative errors in the observation vector b can be magnified in the reconstructed vector x by almost two orders of magnitude. Thus, one could conclude that the reconstruction of all (not only diagonal) elements of ρ can be worse by at least two orders of magnitude in comparison to the corresponding QST methods but assuming the ideal experimental observation approach. In contrast to these tentative conclusions, we will show below that, in fact, the error robustness can be described by the condition number $\kappa \approx 1$ for both partial and complete tomographic methods.

Analogously to the theoretical approach, we can also optimize the set of rotations of ρ and measure only some peaks of the M_z spectra if some nonideal experimental observation approach is applied. Here we analyze the optimization of rotations for the CYCLOPS method.

First, we optimize the value of the scaling factor s in $A \equiv A_{\mathrm{diag}}^{\mathrm{temp3}}$. By choosing $s \in (0.1, 0.25)$, we find that $\kappa(A^T A) = 6.1375$, which is almost one order smaller than $\kappa(A^T A)$ for $s = 1$. Now, we apply the sets of rotations $R_{\mathrm{diag}}^{\mathrm{opt1}}$ and $R_{\mathrm{diag}}^{\mathrm{opt2}}$ to obtain the coefficient matrices $\bar{A}_{\mathrm{diag}}^{\mathrm{opt1}}$ and $\bar{A}_{\mathrm{diag}}^{\mathrm{opt2}}$ assuming the scaling factors $s = 0.2318$ and $s = 0.3043$, respectively. Specifically, the optimal value of s for a given coefficient matrix A is chosen here as $\max_{i,j} A'_{ij}$, where A' is the matrix A but without the last row (i.e., with the nonzero elements equal to s). Note that this last equation is added to include the normalization condition for measuring the nth peak ($n = 1,2$) using the CYCLOPS method. Although our precise expressions for the coefficient matrices $\bar{A}_{\mathrm{diag}}^{\mathrm{opt1}}$ and $\bar{A}_{\mathrm{diag}}^{\mathrm{opt2}}$ are quite lengthy, and thus are not

shown here, we find that

$$\bar{A}_{\mathrm{diag}}^{\mathrm{opt1}} \approx A_{\mathrm{diag}}^{\mathrm{opt1}} \cong A_{\mathrm{diag}}^{\mathrm{opt2}} \approx \bar{A}_{\mathrm{diag}}^{\mathrm{opt2}}, \tag{56}$$

where Eq. (50) was used. Our precise calculations result in the following condition numbers:

$$\begin{aligned} \kappa(A^T A) &= 1.0371 \quad \text{for } A = \bar{A}_{\mathrm{diag}}^{\mathrm{opt1}}, \\ \kappa(A^T A) &= 1.0384 \quad \text{for } A = \bar{A}_{\mathrm{diag}}^{\mathrm{opt2}}, \end{aligned} \tag{57}$$

which are very close to 1.

VIII. RECONSTRUCTION OF THE OFF-DIAGONAL ELEMENTS OF ρ

Now we propose several sets of rotations for the reconstruction of all the off-diagonal terms ρ_{nm} (with $n \neq m$) for the three observation approaches and study the robustness of these methods against errors.

A. Theoretical approach

Our first temporary proposal for QST of a spin-3/2 system is based on a natural choice of 12 rotations (see also Fig. 6):

$$\begin{aligned} R_{\mathrm{offdiag}}^{\mathrm{temp}} = [&Y_{01}, X_{01}, Y_{12}, X_{12}, Y_{23}, X_{23}, Y_{02}, \\ &X_{02}, Y_{13}, X_{13}, Y_{03}, X_{03}], \end{aligned} \tag{58}$$

where hereafter $X_{mn} \equiv \mathcal{X}_{mn}(\tfrac{\pi}{2})$ and $Y_{mn} \equiv \mathcal{Y}_{mn}(\tfrac{\pi}{2})$ as special cases of the selective rotations $\mathcal{X}_{mn}(\theta)$ and $\mathcal{Y}_{mn}(\theta)$ defined in Appendix A. Thus, the method is based on 6 single-photon, 4 two-photon, and 2 three-photon transitions.

In the M_z-detection approach, we can determine the diagonal elements $[\rho_{00}, \rho_{11}, \rho_{22}, \rho_{33}]$ of a density matrix ρ. By denoting the diagonal elements of $\rho^{(k)}$ as $\mathrm{diag}(\rho^{(k)}) \equiv (\rho_{nn}^{(k)})_n$,
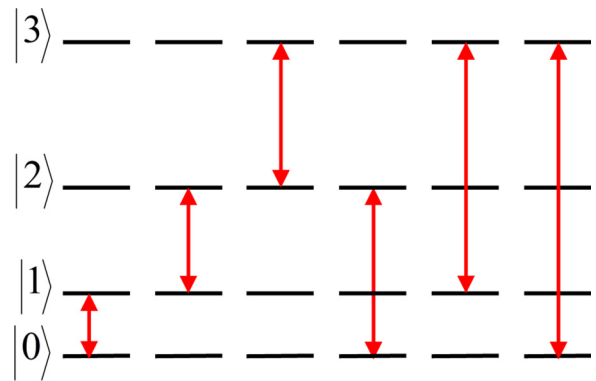

FIG. 6. (Color online) Set of rotations $R_{\mathrm{offdiag}}^{\mathrm{temp}}$ given in Eq. (58), for the reconstruction of all the off-diagonal elements of ρ in the 12 series of measurements by applying the $\pi/2$ pulses: $X_{nm} = \mathcal{X}_{nm}(\pi/2)$ and $Y_{nm} = \mathcal{Y}_{nm}(\pi/2)$, which are in both cases marked by the red double arrows. In the theoretical approach, the off-diagonal elements can directly be obtained by Eq. (61), which implies that the method is optimal with $\kappa = 1$. However, this is not the optimal method assuming the experimental approaches, where only some of the off-diagonal elements can directly be measured, according Eq. (63), while other elements are calculated indirectly, which results in $\kappa > 1$.

the following elements:

$$\mathrm{diag}(\rho^{(1)}) = \left[f_{01}^{(22)}, f_{01}^{(00)}, \rho_{22}, \rho_{33}\right],$$

$$\mathrm{diag}(\rho^{(2)}) = \left[f_{01}^{(13)}, f_{01}^{(31)}, \rho_{22}, \rho_{33}\right],$$

$$\mathrm{diag}(\rho^{(3)}) = \left[\rho_{00}, f_{12}^{(22)}, f_{12}^{(00)}, \rho_{33}\right],$$

$$\mathrm{diag}(\rho^{(4)}) = \left[\rho_{00}, f_{12}^{(13)}, f_{12}^{(31)}, \rho_{33}\right],$$

$$\mathrm{diag}(\rho^{(5)}) = \left[\rho_{00}, \rho_{11}, f_{23}^{(22)}, f_{23}^{(00)}\right],$$

$$\mathrm{diag}(\rho^{(6)}) = \left[\rho_{00}, \rho_{11}, f_{23}^{(13)}, f_{23}^{(31)}\right], \qquad (59)$$

$$\mathrm{diag}(\rho^{(7)}) = \left[f_{02}^{(22)}, \rho_{11}, f_{02}^{(00)}, \rho_{33}\right],$$

$$\mathrm{diag}(\rho^{(8)}) = \left[f_{02}^{(13)}, \rho_{11}, f_{02}^{(31)}, \rho_{33}\right],$$

$$\mathrm{diag}(\rho^{(9)}) = \left[\rho_{00}, f_{13}^{(22)}, \rho_{22}, f_{13}^{(00)}\right],$$

$$\mathrm{diag}(\rho^{(10)}) = \left[\rho_{00}, f_{13}^{(13)}, \rho_{22}, f_{13}^{(31)}\right],$$

$$\mathrm{diag}(\rho^{(11)}) = \left[f_{03}^{(22)}, \rho_{11}, \rho_{22}, f_{03}^{(00)}\right],$$

$$\mathrm{diag}(\rho^{(12)}) = \left[f_{03}^{(13)}, \rho_{11}, \rho_{22}, f_{03}^{(31)}\right],$$

are found for the set of rotations given by Eq. (58), where the auxiliary function $f_{mn}^{(kl)}$ is defined by

$$f_{mn}^{(kl)} = \tfrac{1}{2}(\rho_{mm} + i^k \rho_{mn} + i^l \rho_{nm} + \rho_{nn}). \qquad (60)$$

In the theoretical approach, all these equations can determine the coefficient matrices $A = A_{\mathrm{offdiag}}^{\mathrm{temp}}$, which are based on the set of $N_{\mathrm{eqs}} = 48$ equations given by Eq. (33). The singular values of $C = A^T A$ are found to be $\mathrm{svd}(C) = \{12, 8^{\otimes 3}, 2^{\otimes 12}\}$, where our compact notation $\sigma_i^{\otimes n}$ denotes that σ_i occurs n times. Thus, we can determine the condition number describing the error robustness of the QST method as $\kappa(C) = 6$, which is clearly not optimal. However, by analyzing Eq. (59), one can find that all the off-diagonal elements of ρ can directly be determined as follows:

$$2x_2 = f_{01}^{(00)} - f_{01}^{(22)}, \quad 2x_3 = f_{01}^{(31)} - f_{01}^{(13)},$$

$$2x_9 = f_{12}^{(00)} - f_{12}^{(22)}, \quad 2x_{10} = f_{12}^{(31)} - f_{12}^{(13)},$$

$$2x_{14} = f_{23}^{(00)} - f_{23}^{(22)}, \quad 2x_{15} = f_{23}^{(31)} - f_{23}^{(13)},$$

$$2x_4 = f_{02}^{(00)} - f_{02}^{(22)}, \quad 2x_5 = f_{02}^{(31)} - f_{02}^{(13)}, \qquad (61)$$

$$2x_{11} = f_{13}^{(00)} - f_{13}^{(22)}, \quad 2x_{12} = f_{13}^{(31)} - f_{13}^{(13)},$$

$$2x_6 = f_{03}^{(00)} - f_{03}^{(22)}, \quad 2x_7 = f_{03}^{(31)} - f_{03}^{(13)}.$$

Thus, the corresponding condition number can be decreased to 1.

B. Ideal experimental approach

The M_z-based tomography for the rotations, given by Eq. (58), in the ideal experimental observation approach can be understood as follows: When we apply the Y_{01} pulse after a certain photon operation, we obtain the diagonal components including ρ_{01} and ρ_{10}. In our M_z-detection method, one of the three signals, which corresponds to the differences of the populations between four spin states, is proportional to $\mathrm{Re}(\rho_{01}) + \mathrm{Re}(\rho_{10})$. Because $\rho_{mn} = \rho_{nm}^*$, we can obtain $\mathrm{Re}(\rho_{01}) = \mathrm{Re}(\rho_{10})$. Similarly, $Y_{12}, Y_{23}, Y_{02}, Y_{13}$, and Y_{03} give us

other elements $\mathrm{Re}(\rho_{mn}) = \mathrm{Re}(\rho_{nm})$. Imaginary parts are also estimated by applying the X_{mn} pulse by noting that $\mathrm{Im}(\rho_{mn}) = -\mathrm{Im}(\rho_{nm})$. Although QST needs a few multiphoton operations, this method looks simple and easy to interpret.

In the ideal experimental approach, corresponding to Eq. (34), we obtain $C = A^T A$, where $A = A_{\mathrm{offdiag}}^{\mathrm{temp}}$, having the following singular values:

$$\mathrm{svd}(C) = \{48., 24.25, 16.17, 9.97, 6., 5.45, 5^{\otimes 2},$$
$$4.91, 4.37, 3^{\otimes 2}, 2.92, 2.26, 2, 1.71\}, \qquad (62)$$

which yield the condition number $\kappa(C) = 28.14$, which is far from being optimal.

However, by analyzing the equations in Eq. (59), one can conclude that (at least) some of the off-diagonal terms of ρ can be measured directly, i.e.,

$$b_1^{(1)} = 2x_2, \quad b_1^{(2)} = 2x_3, \quad b_2^{(3)} = 2x_9,$$
$$b_2^{(4)} = 2x_{10}, \quad b_3^{(5)} = 2x_{14}, \quad b_3^{(6)} = 2x_{15}, \qquad (63)$$

where $b_n^{(k)}$ corresponds to the nth peak of the M_z spectrum obtained in the CYCLOPS method for the rotated density matrix $\rho^{(k)} = R_k \rho R_k^\dagger$, where the rotation R_k is given by the kth element in Eq. (58).

In order to directly measure other off-diagonal elements of ρ, one can swap some quartit levels, say, $|k\rangle$ and $|l\rangle$, by applying the π pulse $S_{kl} \equiv \mathcal{Y}_{kl}(\pi)$. For example, one can use the following set of rotations:

$$R_{\mathrm{offdiag}}^{\mathrm{opt0}} = [Y_{01}, X_{01}, Y_{12}, X_{12}, Y_{23}, X_{23}, Y_{01}S_{12}, X_{01}S_{12},$$
$$Y_{12}S_{23}, X_{12}S_{23}, Y_{01}S_{13}, X_{01}S_{13}], \qquad (64)$$

as shown in Fig. 7. Then, all the off-diagonal terms can be directly measured, including

$$b_1^{(7)} = -2x_4, \quad b_1^{(8)} = -2x_5, \quad b_2^{(9)} = -2x_{11},$$
$$b_2^{(10)} = -2x_{12}, \quad b_1^{(11)} = -2x_6, \quad b_1^{(12)} = -2x_7, \qquad (65)$$
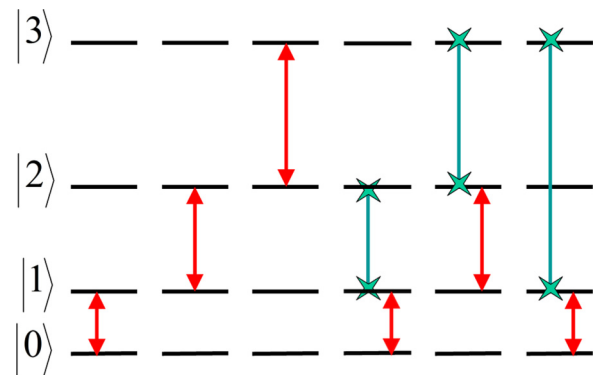

FIG. 7. (Color online) Set of rotations $R_{\mathrm{offdiag}}^{\mathrm{opt0}}$ given in Eq. (64) for the optimal reconstruction of all the off-diagonal elements of ρ. The optimal coefficient matrix $A_{\mathrm{offdiag}}^{\mathrm{opt0}}$ is obtained by measuring only a properly chosen single peak of each M_z spectrum, as indicated in Eqs. (63) and (65).

in addition to those given in Eq. (63). Thus, the corresponding coefficient matrix becomes

$$
A_{\text{offdiag}}^{\text{opt0}} = 2 \begin{pmatrix}
1 & 0 & 0 & 0 & 0 & 0 & 0 & 0 & 0 & 0 & 0 & 0 \\
0 & 1 & 0 & 0 & 0 & 0 & 0 & 0 & 0 & 0 & 0 & 0 \\
0 & 0 & 0 & 0 & 0 & 0 & 1 & 0 & 0 & 0 & 0 & 0 \\
0 & 0 & 0 & 0 & 0 & 0 & 0 & 1 & 0 & 0 & 0 & 0 \\
0 & 0 & 0 & 0 & 0 & 0 & 0 & 0 & 0 & 0 & 1 & 0 \\
0 & 0 & 0 & 0 & 0 & 0 & 0 & 0 & 0 & 0 & 0 & 1 \\
0 & 0 & \bar{1} & 0 & 0 & 0 & 0 & 0 & 0 & 0 & 0 & 0 \\
0 & 0 & 0 & \bar{1} & 0 & 0 & 0 & 0 & 0 & 0 & 0 & 0 \\
0 & 0 & 0 & 0 & 0 & 0 & 0 & 0 & \bar{1} & 0 & 0 & 0 \\
0 & 0 & 0 & 0 & 0 & 0 & 0 & 0 & 0 & \bar{1} & 0 & 0 \\
0 & 0 & 0 & 0 & \bar{1} & 0 & 0 & 0 & 0 & 0 & 0 & 0 \\
0 & 0 & 0 & 0 & 0 & \bar{1} & 0 & 0 & 0 & 0 & 0 & 0
\end{pmatrix},
$$

(66)

where $\bar{1} = -1$. The reconstructed vector for all the off-diagonal elements reads

$$
x = [x_2, x_3, x_4, x_5, x_6, x_7, x_9, x_{10}, x_{11}, x_{12}, x_{14}, x_{15}]^T,
$$

(67)

while the observation vector is

$$
b = \big[b_1^{(1)}, b_1^{(2)}, b_2^{(3)}, b_2^{(4)}, b_3^{(5)}, b_3^{(6)},
$$
$$
b_1^{(7)}, b_1^{(8)}, b_2^{(9)}, b_2^{(10)}, b_1^{(11)}, b_1^{(12)} \big]^T,
$$

(68)

as implied by Eqs. (63) and (65). This observation vector is obtained by measuring only a properly chosen single peak in a given M_z spectrum, while the other two peaks are ignored. Specifically, to determine a chosen term $b_n^{(k)}$, from those in Eqs. (63) and (65), one should only measure the nth peak of the M_z spectra corresponding to the transition $|n-1\rangle \leftrightarrow |n\rangle$ of the rotated density matrix $\rho^{(k)} = R_k \rho R_k^\dagger$, where $R_k = R_{\text{offdiag},k}^{\text{opt0}}$.

We can operationally simplify the problem by requiring that always the same nth peak is measured in the all M_z spectra. For example, to measure always the first peak, one can perform the SWAP-like operations. Thus, we propose the following optimal (in terms of $\kappa = 1$) set of rotations:

$$
R_{\text{offdiag}}^{\text{opt1}} = [Y_{01}, X_{01}, S_{02}Y_{12}, S_{02}X_{12}, Y_{01}S_{13}S_{02},
$$
$$
X_{01}S_{13}S_{02}, Y_{01}S_{12}, X_{01}S_{12}, S_{02}Y_{12}S_{23},
$$
$$
S_{02}X_{12}S_{23}, Y_{01}S_{13}, X_{01}S_{13}],
$$

(69)

as shown in Fig. 8, which corresponds to the following coefficient matrix:

$$
A_{\text{offdiag}}^{\text{opt1}} = 2 \begin{pmatrix}
1 & 0 & 0 & 0 & 0 & 0 & 0 & 0 & 0 & 0 & 0 & 0 \\
0 & 1 & 0 & 0 & 0 & 0 & 0 & 0 & 0 & 0 & 0 & 0 \\
0 & 0 & 0 & 0 & 0 & 0 & \bar{1} & 0 & 0 & 0 & 0 & 0 \\
0 & 0 & 0 & 0 & 0 & 0 & 0 & \bar{1} & 0 & 0 & 0 & 0 \\
0 & 0 & 0 & 0 & 0 & 0 & 0 & 0 & 0 & 0 & 1 & 0 \\
0 & 0 & 0 & 0 & 0 & 0 & 0 & 0 & 0 & 0 & 0 & 1 \\
0 & 0 & \bar{1} & 0 & 0 & 0 & 0 & 0 & 0 & 0 & 0 & 0 \\
0 & 0 & 0 & \bar{1} & 0 & 0 & 0 & 0 & 0 & 0 & 0 & 0 \\
0 & 0 & 0 & 0 & 0 & 0 & 0 & 0 & 1 & 0 & 0 & 0 \\
0 & 0 & 0 & 0 & 0 & 0 & 0 & 0 & 0 & 1 & 0 & 0 \\
0 & 0 & 0 & 0 & \bar{1} & 0 & 0 & 0 & 0 & 0 & 0 & 0 \\
0 & 0 & 0 & 0 & 0 & \bar{1} & 0 & 0 & 0 & 0 & 0 & 0
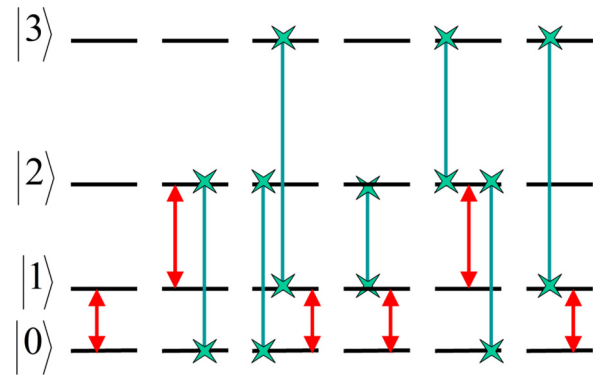\end{pmatrix}.
$$

(70)

FIG. 8. (Color online) Set of rotations $R_{\text{offdiag}}^{\text{opt1}}$ given in Eq. (69) for the optimal reconstruction of all the off-diagonal elements of ρ. Same as in Fig. 6, but the optimal matrix $A_{\text{offdiag}}^{\text{opt1}}$ is obtained by measuring only the first peak of the M_z spectra.

In this approach only the first peak is measured. Alternatively, we can swap the quartit levels in such a way that only the central peak is measured. Then, the optimal tomography can be achieved for the following set of rotations:

$$
R_{\text{offdiag}}^{\text{opt2}} = [Y_{12}S_{02}, X_{12}S_{02}, Y_{12}, X_{12}, Y_{12}S_{13},
$$
$$
X_{12}S_{13}, Y_{12}S_{01}, X_{12}S_{01}, Y_{12}S_{23},
$$
$$
X_{12}S_{23}, Y_{12}S_{01}S_{23}, X_{12}S_{01}S_{23}],
$$

(71)

as shown in Fig. 9, which corresponds to the following coefficient matrix:

$$
A_{\text{offdiag}}^{\text{opt2}} = 2 \begin{pmatrix}
1 & 0 & 0 & 0 & 0 & 0 & 0 & 0 & 0 & 0 & 0 & 0 \\
0 & \bar{1} & 0 & 0 & 0 & 0 & 0 & 0 & 0 & 0 & 0 & 0 \\
0 & 0 & 0 & 0 & 0 & 0 & 1 & 0 & 0 & 0 & 0 & 0 \\
0 & 0 & 0 & 0 & 0 & 0 & 0 & 1 & 0 & 0 & 0 & 0 \\
0 & 0 & 0 & 0 & 0 & 0 & 0 & 0 & 0 & 0 & \bar{1} & 0 \\
0 & 0 & 0 & 0 & 0 & 0 & 0 & 0 & 0 & 0 & 0 & 1 \\
0 & 0 & 1 & 0 & 0 & 0 & 0 & 0 & 0 & 0 & 0 & 0 \\
0 & 0 & 0 & 1 & 0 & 0 & 0 & 0 & 0 & 0 & 0 & 0 \\
0 & 0 & 0 & 0 & 0 & 0 & 0 & 0 & \bar{1} & 0 & 0 & 0 \\
0 & 0 & 0 & 0 & 0 & 0 & 0 & 0 & 0 & \bar{1} & 0 & 0 \\
0 & 0 & 0 & 0 & \bar{1} & 0 & 0 & 0 & 0 & 0 & 0 & 0 \\
0 & 0 & 0 & 0 & 0 & \bar{1} & 0 & 0 & 0 & 0 & 0 & 0
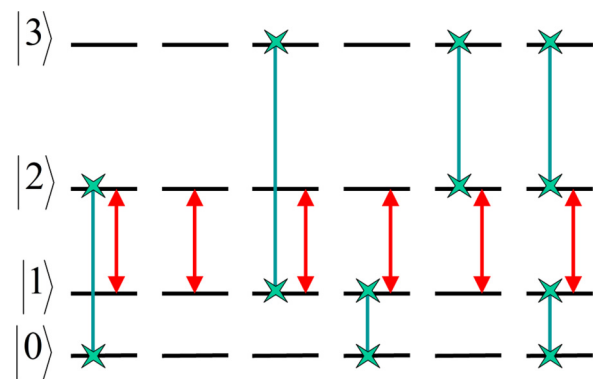\end{pmatrix}.
$$

(72)

FIG. 9. (Color online) Set of rotations $R_{\text{offdiag}}^{\text{opt2}}$ given in Eq. (71). Same as in Fig. 8, but the optimal matrix $A_{\text{offdiag}}^{\text{opt2}}$ is obtained by measuring only the central peak of the M_z spectra.

The advantage of the rotations $R_{\text{offdiag}}^{\text{opt2}}$, in comparison to $R_{\text{offdiag}}^{\text{opt1}}$, resides in the lower number of two-photon rotations. In addition, the remaining two-photon SWAP-like rotations S_{02} and S_{13}, listed in Eq. (71), can be replaced by a sequence of single-photon rotations as described in Sec. X.

It is seen that

$$A_{\text{offdiag}}^{\text{opt0}} \cong A_{\text{offdiag}}^{\text{opt1}} \cong A_{\text{offdiag}}^{\text{opt2}}, \qquad (73)$$

are equivalent up to an irrelevant multiplication of some of their rows by the factor (-1).

In conclusion, we find that the proposed sets of rotations for the reconstruction of all the off-diagonal density-matrix elements in this ideal observation approach are optimal, as leading to the lowest value of the condition number

$$\kappa\left[\left(A_{\text{offdiag}}^{\text{opt},l}\right)^T A_{\text{offdiag}}^{\text{opt},l}\right] = 1 \qquad (74)$$

for $l = 0,1,2$.

C. Nonideal experimental approach via CYCLOPS

The experimental observation approach based on the CYCLOPS method can be considered an imperfect (or noisy) version of the above ideal experimental approach based on Eq. (34). For example, the first peak $b_1^{(1)}$ in the M_z spectrum after the rotation Y_{01} corresponds to:

$$b_1^{(1)} = c_1 x_1 - c_2 x_2 + c_8 x_8 - c_{13} x_{13} - c_{16} x_{13} \approx -c_2 x_2, \quad (75)$$

where $c_1 \approx c_8 \approx 0.0014$, $c_2 \approx 0.4608$, $c_{13} \approx 0.0029$, and $c_{16} \approx 9 \times 10^{-16}$. Note that the element x_2 is dominant, at least by three orders of magnitude in comparison to the other elements, as $c_2 \approx 161 \times \max_{i \neq 2} c_i$. Then we find that the condition number $\kappa(A_{\text{offdiag}}^{\text{opt}}) \approx 1.000$ for the rotations $R_{\text{offdiag}}^{\text{opt},l}$ (for $l = 0,1,2$) assuming the CYCLOPS measurement. This approximate calculation is performed by ignoring the contributions of the diagonal terms x_1, x_8, x_{13}, and x_{16}.

IX. OPTIMAL RECONSTRUCTION OF ALL THE ELEMENTS OF ρ

A. Theoretical approach

By analyzing Eqs. (40) and (61), all of the 16 elements of x (and, thus, ρ) can be accessed directly in this theoretical observation approach. Thereore, the corresponding coefficient matrix is diagonal, and the reconstruction of x is trivial. Thus, this QST is perfectly robust against errors, as the condition number is equal to 1.

B. Ideal experimental approach

In order to reconstruct all the elements of ρ we can combine the optimal reconstructions for the off-diagonal elements (based on the optimal coefficient matrix $A_{\text{offdiag}}^{\text{opt},k}$ corresponding to the rotations $R_{\text{offdiag}}^{\text{opt},k}$ for $k = 0,1,2$) and diagonal elements (described by $A_{\text{diag}}^{\text{opt},l}$ corresponding to $R_{\text{diag}}^{\text{opt},l}$ for $l = 1,2$). For example, the combined coefficient matrices of the dimensions

19×16 can read

$$A_{\text{opt1}} = \left[A_{\text{offdiag}}^{\text{opt1}}; A_{\text{diag}}^{\text{opt1}}\right], \quad A_{\text{opt2}} = \left[A_{\text{offdiag}}^{\text{opt2}}; A_{\text{diag}}^{\text{opt2}}\right], \quad (76)$$

corresponding to the sets of rotations

$$R_{\text{opt1}} = \left[R_{\text{offdiag}}^{\text{opt1}}; R_{\text{diag}}^{\text{opt1}}\right], \quad R_{\text{opt2}} = \left[R_{\text{offdiag}}^{\text{opt2}}; R_{\text{diag}}^{\text{opt2}}\right], \quad (77)$$

respectively. The last row in the matrices in Eq. (76) corresponds to the normalization condition with the scaling factor $s = 1$. Thus, we obtain the total optimal coefficient matrix

$$A_{\text{opt1}} = \begin{pmatrix}
0 & 2 & 0 & 0 & 0 & 0 & 0 & 0 & 0 & 0 & 0 & 0 & 0 & 0 & 0 & 0 \\
0 & 0 & 2 & 0 & 0 & 0 & 0 & 0 & 0 & 0 & 0 & 0 & 0 & 0 & 0 & 0 \\
0 & 0 & 0 & \bar{2} & 0 & 0 & 0 & 0 & 0 & 0 & 0 & 0 & 0 & 0 & 0 & 0 \\
0 & 0 & 0 & 0 & \bar{2} & 0 & 0 & 0 & 0 & 0 & 0 & 0 & 0 & 0 & 0 & 0 \\
0 & 0 & 0 & 0 & 0 & 0 & 0 & 0 & 0 & 0 & 0 & 0 & 0 & 2 & 0 & 0 \\
0 & 0 & 0 & 0 & 0 & 0 & 0 & 0 & 0 & 0 & 0 & 0 & 0 & 0 & 2 & 0 \\
0 & 0 & 0 & \bar{2} & 0 & 0 & 0 & 0 & 0 & 0 & 0 & 0 & 0 & 0 & 0 & 0 \\
0 & 0 & 0 & 0 & \bar{2} & 0 & 0 & 0 & 0 & 0 & 0 & 0 & 0 & 0 & 0 & 0 \\
0 & 0 & 0 & 0 & 0 & 0 & 0 & 0 & 0 & 0 & 2 & 0 & 0 & 0 & 0 & 0 \\
0 & 0 & 0 & 0 & 0 & 0 & 0 & 0 & 0 & 0 & 0 & 2 & 0 & 0 & 0 & 0 \\
0 & 0 & 0 & 0 & 0 & \bar{2} & 0 & 0 & 0 & 0 & 0 & 0 & 0 & 0 & 0 & 0 \\
0 & 0 & 0 & 0 & 0 & 0 & \bar{2} & 0 & 0 & 0 & 0 & 0 & 0 & 0 & 0 & 0 \\
\bar{1} & 0 & 0 & 0 & 0 & 0 & 0 & 1 & 0 & 0 & 0 & 0 & 0 & 0 & 0 & 0 \\
0 & 0 & 0 & 0 & 0 & 0 & 0 & 1 & 0 & 0 & 0 & 0 & \bar{1} & 0 & 0 & 0 \\
0 & 0 & 0 & 0 & 0 & 0 & 0 & 0 & 0 & 0 & 0 & \bar{1} & 0 & 0 & 1 & 0 \\
\bar{1} & 0 & 0 & 0 & 0 & 0 & 0 & 0 & 0 & 0 & 0 & 0 & 0 & 0 & 0 & 1 \\
\bar{1} & 0 & 0 & 0 & 0 & 0 & 0 & 0 & 0 & 0 & 0 & 1 & 0 & 0 & 0 & 0 \\
0 & 0 & 0 & 0 & 0 & 0 & 0 & 1 & 0 & 0 & 0 & 0 & 0 & 0 & 0 & \bar{1} \\
s & 0 & 0 & 0 & 0 & 0 & 0 & s & 0 & 0 & 0 & 0 & s & 0 & 0 & s
\end{pmatrix}, \qquad (78)$$

where $\bar{1} = -1$ and $\bar{2} = -2$. For brevity, the analogous coefficient matrix A_{opt2} is not presented here. A simple calculation shows that $C_{\text{opt},l} = (A_{\text{opt},l})^\dagger A_{\text{opt},l}$ (for $l = 1,2$) is proportional to the identity operator, so the condition number $\kappa(C_{\text{opt},l}) = 1$. Thus, the proposed tomographic methods are optimal concerning their robustness against errors assuming the ideal experimental observations.

C. Nonideal experimental approach using CYCLOPS

In the nonideal experimental approach, we can follow the analysis for the ideal experimental approach. In particular, we can apply Eq. (78) but for the properly chosen scaling factors. It should be stressed that Eq. (78) is only an approximation of $\bar{A}_{\text{opt1}}$ for the nonideal case. For example, the first row for exact $\bar{A}_{\text{opt1}}$ is given by Eq. (75). However, we observe that

$$\bar{A}_{\text{opt1}} \approx A_{\text{opt1}} \cong A_{\text{opt2}} \approx \bar{A}_{\text{opt2}}, \qquad (79)$$

where the combined coefficient matrices $\bar{A}_{\text{opt},l}$ (for $l = 1,2$) are obtained for the sets of rotations $R_{\text{opt},l}$, given in Eq. (77), analogously to $A_{\text{opt},l}$, given in Eq. (76). Note that the last row in $\bar{A}_{\text{opt1}}$ and $\bar{A}_{\text{opt2}}$ corresponds to the normalization condition with the scaling factors $s = 0.2304$ and $s = 0.3043$, respectively. Moreover, in the solution $x = A^{-1}b$, the observation vector b is equal to $[b_l^{(1)}, b_l^{(2)}, \ldots, b_l^{(18)}, 0]^T$ for $l = 1,2$, respectively, and the reconstructed state vector $x = [x_1, x_2, \ldots, x_{16}]^T - \frac{1}{4}$ is related to ρ by Eq. (25). By performing precise numerical calculations, we conclude that the condition numbers are very

close 1, i.e.,

$$\kappa(A^T A) = 1.0592 \approx 1 \quad \text{for } A = \bar{A}_{\text{opt1}},$$
$$\kappa(A^T A) = 1.0528 \approx 1 \quad \text{for } A = \bar{A}_{\text{opt2}}. \tag{80}$$

Thus, even the nonideal QST, as based on the CYCLOPS method, can be almost perfectly robust to errors, as described by their condition numbers κ.

X. SINGLE-PHOTON REPLACEMENTS FOR MULTIPHOTON ROTATIONS

The error-robustness analysis is based on the properties of the coefficient matrices A and, thus, enables us to find experimental setups for the reliable QST even without specific experimental data. The optimization in our approach resides in replacing degenerate multiphoton (multiquantum) rotations by single-photon ones.

For example, some of the discussed sets of rotations for QST include single-photon X rotations (X_{01}, X_{12}, X_{23}), two-photon X rotations (X_{02}, X_{13}), and a three-photon X rotation (X_{03}) together with analogous Y rotations. In particular, the three-photon transitions are not the simplest to be realized experimentally due to the degeneracy between $\omega_{03}/3$ and ω_{12} if the second-order quadrupolar shifts are neglected (see Fig. 1). Namely, we want to perform the three-photon rotations Y_{03} and X_{03} between levels $|0\rangle$ and $|3\rangle$ (for brevity, we say the 0-3 rotation) solely without changing populations between levels $|1\rangle$ and $|2\rangle$. We can effectively rotate 1-2 without rotating 0-3, but we are not able to rotate 0-3 without rotating 1-2. So a feasible tomographic method should be described without direct rotations 0-3. Under this requirement, it is easy to show analytically that one needs combinations of at least two rotations for some of the operations for complete reconstruction. Then, unfortunately, the above interpretation of the tomographic operations, given by Eq. (59), loses its clarity.

First, we calculate replacements for multiphoton X rotations. By inspection, we find that

$$\mathcal{X}_{0n}(\theta) = S_{1n} \mathcal{X}_{01}(\theta) S_{1n}^\dagger = S_{01} \mathcal{X}_{1n}(-\theta) S_{01}^\dagger$$
$$= S_{02} \mathcal{X}_{2n}(-\theta) S_{02}^\dagger = S_{2n} \mathcal{X}_{02}(\theta) S_{2n}^\dagger$$
$$= S_{01} S_{2n} \mathcal{X}_{12}(-\theta) S_{2n}^\dagger S_{01}^\dagger, \tag{81}$$

given in terms of SWAP-like operations $S_{kl} \equiv \mathcal{Y}_{kl}(\pi)$. Note that $\mathcal{Y}_{k,n}^T(\theta) = \mathcal{Y}_{k,n}^\dagger(\theta) = \mathcal{Y}_{k,n}(-\theta)$, so $S_{kl}^\dagger = \mathcal{Y}_{kl}(-\pi)$. Analogously, other replacements can be found. By repeatedly applying the first relation in Eq. (81) we obtain a general formula for any two levels $k < n - 1$:

$$\mathcal{X}_{kn}(\theta) = S_{k+1,n} \mathcal{X}_{k,k+1}(\theta) S_{k+1,n}^\dagger. \tag{82}$$

Alternatively, one can apply the second relation in Eq. (81) to obtain:

$$\mathcal{X}_{kn}(\theta) = S^{(k,n)} \mathcal{X}_{n-1,n}[(-1)^{n-k+1}\theta] (S^{(k,n)})^\dagger, \tag{83}$$

where

$$S^{(k,n)} \equiv S_{k,k+1} S_{k+1,k+2} \cdots S_{n-2,n-1}. \tag{84}$$

In the same way, we find replacements for multiphoton Y rotations for any θ and $k < n - 1$:

$$\mathcal{Y}_{kn}(\theta) = S_{k+1,n} \mathcal{Y}_{k,k+1}(\theta) S_{k+1,n}^\dagger$$
$$= S^{(k,n)} \mathcal{Y}_{n-1,n}[(-1)^{n-k+1}\theta] (S^{(k,n)})^\dagger, \tag{85}$$

in terms of the pulse sequences given by Eq. (84).

In a special case, for a given QST method of the quartit system, the X rotations based on three-photon (0-3) and two-photon (0-2 and 1-3) transitions can be replaced by various sequences of rotations requiring only single-photon transitions, e.g.,

$$\mathcal{X}_{03}(\theta) = S_{01} S_{23} \mathcal{X}_{12}(-\theta) S_{23}^\dagger S_{01}^\dagger,$$
$$\mathcal{X}_{02}(\theta) = S_{01} \mathcal{X}_{12}(-\theta) S_{01}^\dagger, \tag{86}$$
$$\mathcal{X}_{13}(\theta) = S_{12} \mathcal{X}_{23}(-\theta) S_{12}^\dagger,$$

and analogously for the multiquantum Y rotations.

Finally, we point out some practical aspects in the described realization of a nanometer-scale device in a relation to the problem of degeneracy between $\omega_{03}/3$ and ω_{12}. The rotation frequency is proportional to the first Bessel function of the oscillation field strength for the coherent rotation between levels $|1\rangle$ and $|2\rangle$ but proportional to the third Bessel function for that between $|0\rangle$ and $|3\rangle$. Therefore, the 0-3 rotation becomes negligible if the applied field is weak. Moreover, it is possible to select the oscillating field strength, which satisfies some angle rotation for 0-3, which differs from a multiple of 2π rotation for 2-3. Therefore, it is possible to realize a pure 0-3 operation without 2-3 rotation. However, the current amplitude necessary for this operation might be very high and the operation is not realistic from the viewpoint of heating. Another QST method based on sequences of the two-photon pulses $X_{02}, X_{13}, Y_{02},$ and Y_{13} would also be experimentally feasible. But, usually, rotations between the closest levels are much faster and easier to perform.

Here we give a simple solution to omit rotations requiring three-photon transitions in, e.g., the rotations $R_{\text{offdiag}}^{\text{temp}}$ is to express them as combinations of three one-photon and two-photon rotations as described above. However, we find that combinations of only two rotations are usually sufficient. Thus, we suggest the following three-photon rotations: $Y_{03} \rightarrow Y_{01} S_{13}$ and $X_{03} \rightarrow X_{01} S_{13}$. Note that the new operations do not require the rotation 0-3. We mention that the two-photon transitions can also be replaced by single-photon transitions with the help of the sequences of rotations given by Eq. (86).

XI. CONCLUSIONS

We described various methods for implementing quantum state tomography for systems of quadrupolar nuclei with spin-3/2 (equivalent to quartit) in an unconventional approach to NMR, which is based on the measurement of longitudinal magnetization M_z instead of the standard measurement of the transverse magnetization M_{xy} [63].

This work has been motivated by the demonstration of high-precision M_z-based NMR techniques of coherent manipulation of nuclear spins $I = 3/2$ (^{69}Ga, ^{71}Ga, and ^{75}As) in a GaAs quantum-well device based on an the fractional quantum Hall effect [42]. The device, exhibiting extremely low

decoherence [44], offers new possibilities to study interactions in semiconductors but also enables the realization of single- and two-qubit quantum gates [33] and, possibly, testing simple quantum-information processing algorithms.

Although our presentation of the protocols of QST of large-nuclear systems was focused on the nanoscale semiconductor device of Ref. [42], it should be stressed that these protocols can also be readily applied to large-nuclear spins in other systems.

We proposed methods with optimized sets of rotations. The optimization was applied in order to improve the robustness against errors, as quantified by condition numbers.

Some of the proposed QST methods for a quartit system require the three-photon transitions (between levels $|0\rangle$ and $|3\rangle$), which are induced by relatively strong pulses. Unfortunately, such pulses can simultaneously induce transitions between levels $|1\rangle$ and $|2\rangle$. Thus, from a practical point of view, it is desired to apply only weak pulses selectively inducing single-photon transitions. We showed how the rotations requiring multiphoton transitions can be replaced by combinations of rotations based only on single-photon transitions.

By applying the condition number based on the spectral norm [56], we compared robustness against errors in the measured data for all the described tomographic methods. We have assumed three observation approaches corresponding to: (i) an ideal M_z detection, where all the diagonal elements ρ_{nn} ($n = 0, \ldots, 3$) of a density matrix can be directly accessed; (ii) an ideal experimental M_z detection, where the population differences ($\rho_{11} - \rho_{00}$, $\rho_{22} - \rho_{11}$, and $\rho_{33} - \rho_{22}$) can be estimated from the amplitude of the signals by integrating the area of the peaks centered at ω_{01}, ω_{12}, and ω_{23} (see Fig. 2), respectively; and (iii) the nonideal ("noisy") experimental detection based on the CYCLOPS method, where the information gathered from the M_z spectra corresponds to some linear functions of the diagonal elements ρ_{nn}, as given by Eq. (37).

For the QST methods for a quartit (i.e., two virtual qubits) using the experimental approaches (including the CYCLOPS method), the condition number κ is either exactly equal to 1 or very close to 1. This means that the proposed methods are optimally robust against errors.

Let us now compare the error robustness of the discussed NMR QST methods with some known optical QST methods (see, e.g., Ref. [8] for a review) for two physically distinct qubits: The well-known QST protocol of James *et al.* [4], which is solely based on local measurements, yields the condition number $\kappa = 60.1$. The QST of Refs. [5,6] is based on the standard separable basis composed of all of the 36 two-qubit eigenstates of the tensor products of the Pauli operators. This often-applied QST yields $\kappa = 9$. Another QST, which is based on local measurements of the 16 tensor products of the Pauli operators, yields $\kappa = 2$. In contrast to these optical methods, only the recently proposed QST of Ref. [8], which was also experimentally demonstrated [64], is optimal since it yields the condition number $\kappa = 1$. This tomography of two optical qubits is based on local and global measurements of generalized Pauli operators. It is worth noting that our optimal NMR tomography is based on a smaller set of measurements in comparison to that for the optimal optical tomography [8,64].

We also described sequences of NMR pulses to perform various quantum tomography methods and arbitrary gates

(including single virtual qubit rotations) with nuclear spins-3/2. This enables a simple translation of arbitrary quantum algorithms from systems of spins-1/2 to higher-number spins.

Finally, we express our hope that this comparative study of various NMR tomographic methods will draw attention to the issue of how such methods are robust against errors and, thus, to the question about the reliability of the reconstructed density matrices.

APPENDIX A: SELECTIVE ROTATIONS

Selective rotations in quadrupolar nuclei with large spins are a simple generalization of the standard rotations in a spin-1/2 system:

$$\mathcal{X}(\theta) \equiv R^x(\theta) = \begin{bmatrix} \cos\frac{\theta}{2} & -i\sin\frac{\theta}{2} \\ -i\sin\frac{\theta}{2} & \cos\frac{\theta}{2} \end{bmatrix}, \quad \text{(A1)}$$

$$\mathcal{Y}(\theta) \equiv R^y(\theta) = \begin{bmatrix} \cos\frac{\theta}{2} & -\sin\frac{\theta}{2} \\ \sin\frac{\theta}{2} & \cos\frac{\theta}{2} \end{bmatrix}, \quad \text{(A2)}$$

$$\mathcal{Z}(\theta) \equiv R^z(\theta) = \begin{bmatrix} e^{-i\theta/2} & 0 \\ 0 & e^{i\theta/2} \end{bmatrix}. \quad \text{(A3)}$$

If a two-level rotation is $R^{(i)}(\theta) = \begin{bmatrix} a & b \\ c & d \end{bmatrix}$ (with $i = X, Y, Z$), then the corresponding selective rotation between levels $m < n$ in a N-level system is given by

$$R_{mn}^{(i)}(\theta) = a|m\rangle\langle m| + b|m\rangle\langle n| + c|n\rangle\langle m|$$
$$+ d|n\rangle\langle n| + \sum_{k \neq n,m} |k\rangle\langle k|. \quad \text{(A4)}$$

For example, the matrix representation of the rotation $\mathcal{X}_{02}(\frac{\pi}{2})$ in a spin-3/2 system reads as:

$$\mathcal{X}_{02}\left(\frac{\pi}{2}\right) = \frac{1}{\sqrt{2}} \begin{pmatrix} 1 & 0 & -i & 0 \\ 0 & \sqrt{2} & 0 & 0 \\ -i & 0 & 1 & 0 \\ 0 & 0 & 0 & \sqrt{2} \end{pmatrix}. \quad \text{(A5)}$$

Note that the rotations calculated by $\exp(-i\mathcal{H}_{\text{rot}}t_p/\hbar)$ are, in general, not exactly corresponding to Eq. (A4), because

these depend on the quadrupolar frequency ω_Q, even if the conditions $\hbar\omega_{RF}^{(k)} = \epsilon_m - \epsilon_n$ and $|\omega_k| \ll |\omega_Q| \ll |\omega_0|$ are satisfied [49]. Nevertheless, these rotations can be effectively reduced to Eq. (A4) if the pulse duration t_p is equal to $2\pi/\omega_Q$ or its multiple. To fulfill this condition experimentally, the line intensities of spectra can be monitored as a function of the pulse duration (see, e.g., Ref. [16]).

APPENDIX B: M_{xy} DETECTION VS M_z DETECTION

The M_{xy}-detection of a spin-3/2 system provides directly the following off-diagonal elements (as marked in boxes) of the corresponding density matrix ρ:

$$\rho = \begin{bmatrix} \rho_{00} & \boxed{\rho_{01}} & \rho_{02} & \rho_{03} \\ \boxed{\rho_{10}} & \rho_{11} & \boxed{\rho_{12}} & \rho_{13} \\ \rho_{20} & \boxed{\rho_{21}} & \rho_{22} & \boxed{\rho_{23}} \\ \rho_{30} & \rho_{31} & \boxed{\rho_{32}} & \rho_{33} \end{bmatrix}. \tag{B1}$$

This is because the NMR signals obtained by the M_{xy} detection can be proportional to [63]

$$M_{xy}^{\pm} \equiv M_x \pm \mathrm{i}M_y \ \propto \ \mathrm{Tr}[\rho I_{\pm}], \tag{B2}$$

as given in terms of the total angular-momentum operator $I_{\pm} = I_x \pm iI_y$ for spin $I = 3/2$, where

$$I_x = \begin{bmatrix} 0 & a & 0 & 0 \\ a & 0 & 1 & 0 \\ 0 & 1 & 0 & a \\ 0 & 0 & a & 0 \end{bmatrix}, \quad I_y = i \begin{bmatrix} 0 & -a & 0 & 0 \\ a & 0 & -1 & 0 \\ 0 & 1 & 0 & -a \\ 0 & 0 & a & 0 \end{bmatrix}, \tag{B3}$$

with $a = \sqrt{3}/2$. In contrast to this, the M_z detection of a spin-3/2 system and two spin-1/2 systems enables the determination of only the diagonal elements ρ_{ii} ($i = 0, \ldots, 3$). This is because the NMR signals obtained by the M_z detection of a spin-3/2 system are given by Eqs. (34), (35), or (37).

[1] W. P. Schleich and H. Walther, *Elements of Quantum Information* (Wiley-VCH, Weinheim, 2007).

[2] M. G. A. Paris and J. Řeháček (eds.), *Quantum State Estimation*, Lecture Notes in Physics, Vol. 649 (Springer, Berlin, 2004).

[3] G. M. D'Ariano, M. G. A. Paris, and M. F. Sacchi, Quantum tomography, Adv. Imag. Elect. Phys. **128**, 205 (2003).

[4] D. F. V. James, P. G. Kwiat, W. J. Munro, and A. G. White, Measurement of qubits, Phys. Rev. A **64**, 052312 (2001).

[5] J. B. Altepeter, E. R. Jeffrey, and P. G. Kwiat, Phase-compensated ultra-bright source of entangled photons, Opt. Express **13**, 8951 (2005).

[6] M. D. de Burgh, N. K. Langford, A. C. Doherty, and A. Gilchrist, Choice of measurement sets in qubit tomography, Phys. Rev. A **78**, 052122 (2008).

[7] R. B. A. Adamson and A. M. Steinberg, Improving Quantum State Estimation with Mutually Unbiased Bases, Phys. Rev. Lett. **105**, 030406 (2010).

[8] A. Miranowicz, K. Bartkiewicz, J. Peřina Jr., M. Koashi, N. Imoto, and F. Nori, Optimal two-qubit tomography based on local and global measurements: Maximal robustness against errors as described by condition numbers, Phys. Rev. A **90**, 062123 (2014).

[9] K. Vogel and H. Risken, Determination of quasiprobability distributions in terms of probability distributions for the rotated quadrature phase, Phys. Rev. A **40**, 2847(R) (1989).

[10] K. Lobino, D. Korystov, C. Kupchak, E. Figueroa, B. C. Sanders, and A. I. Lvovsky, Complete characterization of quantum-optical processes, Science **322**, 563 (2008); S. Rahimi-Keshari, A. Scherer, A. Mann, A. T. Rezakhani, A. I. Lvovsky, and B. C. Sanders, Quantum process tomography with coherent states, New J. Phys. **13**, 013006 (2011).

[11] X. B. Wang, Z. W. Yu, J.-Z. Hu, A. Miranowicz, and F. Nori, Efficient tomography of quantum optical Gaussian processes probed with a few coherent states, Phys. Rev. A **88**, 022101 (2013).

[12] J. Q. You and F. Nori, Superconducting circuits and quantum information, Phys. Today **58**, 42 (2005); Atomic physics and quantum optics using superconducting circuits, Nature **474**, 589 (2011).

[13] Y. X. Liu, L. F. Wei, and F. Nori, Quantum tomography for solid state qubits, Europhys. Lett. **67**, 874 (2004); Tomographic measurements on superconducting qubit states, Phys. Rev. B **72**, 014547 (2005); M. Steffen *et al.*, State Tomography of Capacitively Shunted Phase Qubits with High Fidelity, Phys. Rev. Lett. **97**, 050502 (2006).

[14] J. A. Jones, Quantum computing with NMR, Prog. Nucl. Mag. Res. Spectr. **59**, 91 (2011).

[15] L. M. K. Vandersypen and I. L. Chuang, NMR techniques for quantum control and computation, Rev. Mod. Phys. **76**, 1037 (2005), and references therein.

[16] F. A. Bonk *et al.*, Quantum-state tomography for quadrupole nuclei and its application on a two-qubit system, Phys. Rev. A **69**, 042322 (2004); Quantum logical operations for spin 3/2 quadrupolar nuclei monitored by quantum state tomography, J. Magn. Reson. **175**, 226 (2005).

[17] H. Kampermann and W. S. Veeman, Characterization of quantum algorithms by quantum process tomography using quadrupolar spins in solid-state nuclear magnetic resonance, J. Chem. Phys. **122**, 214108 (2005).

[18] R. Auccaise, J. Teles, R. S. Sarthour, T. J. Bonagamba, I. S. Oliveira and E. R. deAzevedo, A study of the relaxation dynamics in a quadrupolar NMR system using quantum state tomography, J. Magn. Reson. **192**, 17 (2008).

[19] J. Teles, E. R. deAzevedo, J. C. C. Freitas, R. S. Sarthour, I. S. Oliveira, and T. J. Bonagamba, Quantum information processing by nuclear magnetic resonance on quadrupolar nuclei, Phil. Trans. Math. Phys. Eng. Sci. **370**, 4770 (2012).

[20] J. Teles, E. R. deAzevedo, R. Auccaise, R. S. Sarthour, I. S. Oliveira, and T. J. Bonagamba, Quantum state tomography for quadrupolar nuclei using global rotations of the spin system, J. Chem. Phys. **126**, 154506 (2007).

[21] F. Nori, Quantum Football, Science **325**, 689 (2009); M. Neeley *et al.*, Emulation of a quantum spin with a superconducting phase qudit, *ibid.* **325**, 722 (2009).

[22] B. Lanyon *et al.*, Simplifying quantum logic using higher-dimensional Hilbert spaces, Nat. Phys. **5**, 134 (2009).

[23] M. N. Leuenberger and D. Loss, Quantum computing in molecular magnets, Nature (London) **410**, 789 (2001).

[24] A. Ardavan, O. Rival, J. J. L. Morton, S. J. Blundell, A. M. Tyryshkin, G. A. Timco, R. E. P. Winpenny, Will spin-relaxation times in molecular magnets permit quantum information processing?, Phys. Rev. Lett. **98**, 057201 (2007).

[25] A. K. Khitrin and B. M. Fung, Nuclear magnetic resonance quantum logic gates using quadrupolar nuclei, J. Chem. Phys. **112**, 6963 (2000).

[26] N. Sinha, T. S. Mahesh, K. V. Ramanathan, and A. Kumar, Toward quantum information processing by nuclear magnetic resonance: Pseudopure states and logical operations using selective pulses on an oriented spin 3/2 nucleus, J. Chem. Phys. **114**, 4415 (2001).

[27] A. Kumar, K. Ramanathan, T. Mahesh, N. Sinha, and K. Murali, Developments in quantum information processing by nuclear magnetic resonance: Use of quadrupolar and dipolar couplings, J. Phys. Pramana **59**, 243 (2002).

[28] R. S. Sarthour *et al.*, Relaxation of coherent states in a two-qubit NMR quadrupole system, Phys. Rev. A **68**, 022311 (2003).

[29] H. Kampermann and W. S. Veeman, Quantum computing using quadrupolar spins in solid state NMR, Quantum Inf. Process. **1**, 327 (2002).

[30] V. L. Ermakov and B. M. Fung, Experimental realization of a continuous version of the Grover algorithm, Phys. Rev. A **66**, 042310 (2002).

[31] R. Das and A. Kumar, Use of quadrupolar nuclei for quantum-information processing by nuclear magnetic resonance: Implementation of a quantum algorithm, Phys. Rev. A **68**, 032304 (2003).

[32] D. O. Soares-Pinto, L. C. Céleri, R. Auccaise, F. F. Fanchini, E. R. deAzevedo, J. Maziero, T. J. Bonagamba, and R. M. Serra, Nonclassical correlation in NMR quadrupolar systems, Phys. Rev. A **81**, 062118 (2010).

[33] Y. Hirayama, A. Miranowicz, T. Ota, G. Yusa, K. Muraki, Ş. K. Özdemir, and N. Imoto, Nanometre-scale nuclear-spin device for quantum information processing, J. Phys.: Condens. Matter **18**, S885 (2006); Ş. K. Özdemir, A. Miranowicz, T. Ota, G. Yusa, N. Imoto, and Y. Hirayama, Nuclear spins in a nanoscale device for quantum information processing, e-J. Surf. Sci. Nanotech. **4**, 669 (2006).

[34] Y. P. Tan, X. F. Nie, J. Li, H. W. Chen, X. Y. Zhou, X. H. Peng, and J. F. Du, Preparing pseudo-pure states in a quadrupolar spin system using optimal control, Chin. Phys. Lett. **29**, 127601 (2012).

[35] A. K. Khitrin, H. Sun, and B. M. Fung, Method of multi-frequency excitation for creating pseudopure states for NMR quantum computing, Phys. Rev. A **63**, 020301(R) (2001).

[36] A. K. Khitrin and B. M. Fung, NMR simulation of an eight-state quantum system, Phys. Rev. A **64**, 032306 (2001).

[37] K. V. R. M. Murali, N. Sinha, T. S. Mahesh, M. H. Levitt, K. V. Ramanathan, and A. Kumar, Quantum-information processing by nuclear magnetic resonance: Experimental implementation of half-adder and subtractor operations using an oriented spin-7/2 system, Phys. Rev. A **66**, 022313 (2002).

[38] K. V. R. M. Murali, H. B. Son, M. Steffen, P. Judeinstein, and I. L. Chuang, Test by NMR of the phase coherence of electromagnetically induced transparency, Phys. Rev. Lett. **93**, 033601 (2004).

[39] R. Das and A. Kumar, Experimental implementation of a quantum algorithm in a multiqubit NMR system formed by an oriented 7/2 spin, Appl. Phys. Lett. **89**, 024107 (2006).

[40] T. Gopinath and A. Kumar, Implementation of controlled phase shift gates and Collins version of Deutsch-Jozsa algorithm on a quadrupolar spin-7/2 nucleus using non-adiabatic geometric phases, J. Magn. Reson. **193**, 168 (2008).

[41] T. Machida, T. Yamazaki, K. Ikushima, and S. Komiyama, Coherent control of nuclear-spin system in a quantum-Hall device, Appl. Phys. Lett. **82**, 409 (2003); T. Takahashi *et al.*, Electrical coherent control of nuclear spins in a breakdown regime of quantum Hall effect, *ibid.* **91**, 092120 (2007).

[42] G. Yusa, K. Muraki, K. Takashina, K. Hashimoto, and Y. Hirayama, Controlled multiple quantum coherences of nuclear spins in a nanometre-scale device, Nature (London) **434**, 1001 (2005).

[43] T. Ota, G. Yusa, N. Kumada, S. Miyashita, and Y. Hirayama, Nuclear spin population and its control toward initialization using an all-electrical submicron scale nuclear magnetic resonance device, Appl. Phys. Lett. **90**, 102118 (2007); T. Ota, G. Yusa, N. Kumada, S. Miyashita, T. Fujisawa, and Y. Hirayama, Initialization and logic gate operations of nuclear spin qubits using a submicron scale resistively-detected NMR device, Phys. Stat. Sol. (c) **5**, 306 (2008).

[44] T. Ota, G. Yusa, N. Kumada, S. Miyashita, T. Fujisawa, and Y. Hirayama, Decoherence of nuclear spins due to direct dipole-dipole interactions probed by resistively detected nuclear magnetic resonance, Appl. Phys. Lett. **91**, 193101 (2007); T. Ota, N. Kumada, G. Yusa, T. Fujisawa, Y. Hirayama and S. Miyashita, Coherence time of nuclear spins in GaAs quantum well probed by submicron-scale all-electrical nuclear magnetic resonance device, Jpn. J. Appl. Phys. **47**, 3115 (2008).

[45] Y. Hirayama, G. Yusa, K. Hashimoto, N. Kumada, T. Ota and K. Muraki, Electron-spin/nuclear-spin interactions and NMR in semiconductors, Semicond. Sci. Technol. **24**, 023001 (2009).

[46] Y. Kondo, M. Ono, S. Matsuzaka, K. Morita, H. Sanada, Y. Ohno, and H. Ohno, Multipulse operation and optical detection of nuclear spin coherence in a GaAs/AlGaAs quantum well, Phys. Rev. Lett. **101**, 207601 (2008).

[47] R. T. Thew, K. Nemoto, A. G. White, and W. J. Munro, Qudit quantum-state tomography, Phys. Rev. A **66**, 012303 (2002).

[48] A. Abragam, *Principles of Nuclear Magnetism* (Oxford University Press, London, 1961).

[49] R. R. Ernst, G. Bodenhausen, and A. Wokaun, *Principles of Nuclear Magnetic Resonance in One and Two Dimensions* (Oxford University Press, Oxford, 1987).

[50] M. N. Leuenberger, D. Loss, M. Poggio, and D. D. Awschalom, Quantum information processing with large nuclear spins in GaAs semiconductors, Phys. Rev. Lett. **89**, 207601 (2002); M. N. Leuenberger and D. Loss, The Grover algorithm with large nuclear spins in semiconductors, Phys. Rev. B **68**, 165317 (2003).

[51] M. H. Levitt, *Spin Dynamics: Basics of Nuclear Magnetic Resonance* (Wiley, New York, 2002).

[52] G. Salis, D. D. Awschalom, Y. Ohno, and H. Ohno, Origin of enhanced dynamic nuclear polarization and all-optical nuclear

magnetic resonance in GaAs quantum wells, Phys. Rev. B **64**, 195304 (2001).

[53] K. Hashimoto, K. Muraki, T. Saku and Y. Hirayama, Electrically Controlled Nuclear Spin Polarization and Relaxation by Quantum-Hall States, Phys. Rev. Lett. **88**, 176601 (2002); K. Hashimoto, T. Saku and Y. Hirayama, Nuclear-spin-related resistance enhancements observed over a wide range of magnetic fields, Phys. Rev. B **69**, 153306 (2004).

[54] H. W. Liu, K. F. Yang, T. D. Mishima, M. B. Santos, and Y. Hirayama, Dynamic nuclear polarization and nuclear magnetic resonance in the simplest pseudospin quantum Hall ferromagnet, Phys. Rev. B **82**, 241304(R) (2010).

[55] K. E. Atkinson, *An Introduction to Numerical Analysis* (Wiley, New York, 1989).

[56] N. J. Higham, *Accuracy and Stability of Numerical Algorithms* (SIAM, Philadelphia, 1996).

[57] G. Golub and C. F. van Loan, *Matrix Computations* (Johns Hopkins University Press, Baltimore, 1989).

[58] C. D. Meyer, *Matrix Analysis and Applied Linear Algebra* (SIAM, Philadelphia, 2000).

[59] Yu. I. Bogdanov, G. Brida, M. Genovese, S. P. Kulik, E. V. Moreva, and A. P. Shurupov, Statistical Estimation of the Efficiency of Quantum State Tomography Protocols, Phys. Rev. Lett. **105**, 010404 (2010).

[60] S. S. Roy and T. S. Mahesh, Density matrix tomography of singlet states, J. Magn. Reson. **206**, 127 (2010).

[61] G. L. Long, H. Y. Yan, and Y. Sun, Analysis of density matrix reconstruction in NMR quantum computing, J. Opt. B: Quantum Semiclass. Opt. **3**, 376 (2001).

[62] R. Freeman, *A Handbook of Nuclear Magnetic Resonance* (Longman, Essex, 1997).

[63] C. P. Slichter, *Principles of Magnetic Resonance* (Springer, Berlin, 1996).

[64] K. Bartkiewicz, A. Černoch, K. Lemr, and A. Miranowicz, Priority choice experimental two-qubit tomography: Measuring one by one all elements of density matrices, arXiv:1506.01317.